E-Cigarette Exposure Triggers Distal Lung Cell Injury, Persistent Lung Stress Response, and Anti-viral Immune Suppression

Tanner C. Rivera[1*], Kelly S. Schweitzer[1*], Christina Cornell[1], Jordan Nall[1], Nicholas Egersdorf[1], Courtney Moeder[1], Riley A. Cooney[2], Eszter K. Vladar[2], Steve D. Groshong[1,2], Gregory P. Downey[1,2], James P. Bridges[1,2], Richard Bowen[3], Hong Wei Chu[1,2], Irina Petrache[1,2 #]

[1] Department of Medicine, Division of Pulmonary and Critical Care Medicine, National Jewish Health

[2] Department of Medicine, Division of Pulmonary Sciences and Critical Care Medicine, University of Colorado

[3] Department of Biomedical Sciences, Colorado State University

* These authors equally share the first author position.

Corresponding Author Address: Irina Petrache, MD; 1400 Jackson St, Denver, CO 80206; phone: 303-270-2080; Email: petrachei@njhealth.org

Keywords: Vaping, Influenza virus, Coronavirus, Endothelial, Epithelial, Human, Hamster

Abstract

The mechanisms by which e-cigarette vaping (EV) affects lung health remain unclear. Clinical data from clusters of EV-associated lung injury indicate that EV damages distal lung parenchyma and increases vulnerability to second-hit injury, including respiratory viral infections.

Using human lung endothelial and epithelial cells and precision-cut lung slices, we investigated the mechanisms underlying distal lung cell injury and repair triggered by brief (24-hour) EV exposure. Using RNA sequencing of lung tissue from Golden Syrian hamsters, we evaluated the persistence of lung stress responses (10 days after 5 days of EV exposure and determined the impact of EV on host defense against influenza A virus (IAV) and severe acute respiratory syndrome coronavirus 2 (SARS-CoV-2) infections.

EV disrupted the barrier function of human distal lung cells through JNK stress-response signaling, triggered autophagy with impaired autophagolysosomal degradation, suppressed mTOR signaling and cell proliferation, and culminated in apoptosis. Analysis of transcriptional responses in EV-exposed hamster lungs revealed persistent activation of pathways involving JNK signaling, autophagy, barrier dysfunction, tissue remodeling, and impaired Th1 immunity. EV pre-exposure increased the viral burden of SARS-CoV-2, downregulated antiviral genes (Ifit1, Isg15, Nfkbia), and altered Stat1 and Irf7 immune signaling, while amplifying oxidative stress and IL-12 signaling.

These findings show that short-term EV exposure triggered stress-induced distal lung cell injury with persistent changes in antiviral immunity and molecular pathways associated with tissue remodeling. When sustained, as with habitual EV use, these alterations may increase susceptibility to respiratory viral infections and contribute to the development of chronic lung disease.

Introduction

Electronic cigarette (e-cigarette) vaping (EV) has emerged as a popular alternative to tobacco smoking(1, 2). EV poses important risks to lung health(3, 4), most dramatically reflected in a cluster of cases of acute respiratory failure from EV product use-associated lung injury (EVALI)(5), which was attributed to concurrent EV use with vitamin E or tetrahydro cannabinoid or infection with respiratory viruses(5, 6). This suggests EV predisposes to a second-hit injury of the distal lung, which may include weakening of the epithelial and endothelial lung barriers, thereby inducing acute lung inflammation and edema. Additionally, subtle repetitive lung barrier dysfunction has been implicated in chronic obstructive pulmonary disease (COPD)(7, 8), and pulmonary fibrosis(9, 10). We have shown that both nicotine-containing and nicotine-free EV weakens the lung endothelial cell barrier (11) through unknown mechanisms. EV exposure of primary human small airway epithelial cell (HSAEC) cultures and precision cut human lung slices (PCLS) triggers an exaggerated inflammatory response to viruses, weakening anti-viral signaling(12, 13). EV has been shown to increase angiotensin converting enzyme (ACE2) levels, particularly in male mice(14), which could increase the susceptibility to coronavirus infection. These reports indicate that EV has deleterious effects on the host response to subsequent hits such as respiratory viral infections.

Stress-induced signaling pathways, including c-Jun N-terminal kinase (JNK), are critical regulators of cellular responses to environmental insults like reactive oxygen species or aldehydes, that are present in EV(11). JNK signaling has been linked to increased endothelial and epithelial permeability, impaired repair, cell death, autophagy(15, 16), and inflammation. Although autophagy is a protective mechanism during stress, dysregulated autophagy may cause cell death and barrier dysfunction(17). Prior studies implicating JNK in autophagy in CS-exposed cells suggest a role in EV-induced lung injury (17).

To better understand the acute and chronic effects of EV, most investigations relied on laboratory mice, revealing increased oxidative stress(11, 18), emphysema-like lung remodeling(19, 20), and extrapulmonary fibrosis(21). Further, most studies of EV on human specimens have focused on proximal airways(21). Additional animal modeling, complemented with studies in human distal lung specimens, is essential for bridging knowledge gaps. We study here Golden Syrian hamsters (*Mesocricetus Aureus*) due to human-resembling small airway architecture (22) and inflammatory responses to respiratory viruses, including Severe Acute Respiratory Syndrome coronavirus 2 (SARS-CoV-2)(23). Hamsters respond to acute EV exposure by upregulating airway epithelial inflammatory gene and oxidative stress responses(24), rendering it optimal to study EV effects on lung barriers and responses to influenza A virus (IAV) and SARS-COV-2.

We show that EV triggers a JNK-mediated stress response that impairs distal lung barrier function and autophagy, with effects that persist even after cessation of EV exposure, manifesting as alterations in immune and tissue remodeling pathways that change host responses to acute respiratory viral infections.

Results

Barrier Dysfunction of Endothelial and Epithelial Monolayers Following EV Exposure

Trans-endothelial/epithelial electrical resistance (TEER or TER) measured by Electric Cell-Substrate Impedance Sensing (ECIS) and trans-cellular dextran permeability measured by fluorimetry were recorded over time following EV addition. In primary human lung microvascular endothelial cells (HLMVEC), exposure to EV resulted in a dose-dependent reduction in barrier

function (Figure 1A). When normalized to prior to exposure, TER decreased immediately following EV concentrations (5 mM, 7.5 mM, and 10 mM) that simulate casual vaping in humans, with the 10 mM concentration showing the most profound and sustained effect (Figure 1B). EV impaired hSAEC-KT (25) barrier function in a dose-dependent manner (Figure 1C), with concentrations of 7.5 mM and 10 mM showing the greatest effect. In primary hSAECs differentiated into a pseudostratified layer at the air-liquid interface for 3 weeks, EVs reduced barrier function, as assessed by FITC-labeled dextran transmigration (Figure 1D). The slower kinetics compared to those measured by ECIS in the submerged cells likely reflect differences in assay methodology and sensitivity.

Autophagy in Lung Endothelial and Epithelial Cells Following EV Exposure

Next, we determined the effect of EVs on repair via stress-induced autophagy. In HLMVEC, EV exposure increased levels of LC3B-II (Microtubule-associated protein-1 light chain 3-beta-), with a punctate appearance on immunofluorescence imaging, indicating autophagosome formation (Figure 2 A-B; Supplementary Figure 1A, respectively), and p62/SQSTM1 (Sequestosome 1) (Figure 2 A, C; Supplementary Figure 1B). These data imply that EVs initiate autophagy without the full autophagolysosomal degradation required for adequate autophagic repair. Phospho-S6 (ribosomal protein S6), detected by western blotting, was reduced by EV (Figure 2D), indicating suppressed mTOR (mechanistic Target of Rapamycin) activity, consistent with induction of autophagy. EV reduced cell proliferation, detected by decreased EdU staining and fluorescence microscopy (Figure 2E). Immunofluorescence revealed that EVs increased ceramide levels in plasma membranes and perinuclear regions and increased the translocation of cleaved caspase-3 to the nucleus (Figure 2, F and G), consistent with pro-apoptotic signaling and cellular stress.

In hSAEC1-KT, EV increased LC3B-II and p62/SQSTM1 levels (Figure 3, A-E) and markedly decreased cell proliferation, measured by EdU incorporation (Figure 3F). EV

increased apoptosis, as indicated by increased ceramide staining at the plasma membrane (Figure 3G) and increased cleaved PARP1, cell rounding, and nuclear condensation (Figure 3H). Similar responses were observed in cells exposed to an EV juice condensate (Figure 3I), and in human PCLS exposed to EV (Figure 3J, K). These data indicate that EVs induce distal lung cell autophagy with incomplete autophagosome degradation, reduced cell proliferation, and apoptosis.

JNK Inhibition Improves Barrier Function and Autophagy Completion in EV-Exposed Human Lung Microvascular Endothelial Cells

To determine the mechanism by which EVs trigger incomplete autophagy and barrier dysfunction, we next interrogated the role of MAPK pathways. In HLMVEC, under conditions of decreased barrier integrity induced by EV (7.5 mM), pretreatment with a pan-JNK inhibitor (SP600125, 50 μM) significantly attenuated this effect (Figure 4, A and B), indicating that JNK activation contributes to barrier disruption. Western blotting showed that JNK inhibition significantly reduced EV-induced LC3B and p62/SQSTM1 levels (Figure 4, C and D). Complementary immunofluorescence microscopy showed that transformed HLMVEC pre-treated with a JNK inhibitor, compared with vehicle, had reduced accumulation of p62/SQSTM1 (Figure 4E and F). Co-immunostaining for p62/SQSTM1 and the lysosomal marker LAMP1 (Figure 4F) revealed that in EV-exposed cells, most p62-stained puncta did not colocalize with lysosomes (indicating reduced autophago-lysosomal fusion). While JNK inhibition reduced the abundance of p62-stained puncta, it had no effect on LAMP1-stained lysosomes abundance, suggesting that JNK does not impact lysosomal biogenesis. The EV-induced increase in LC3B-II was significantly reduced by inhibitors of JNK, p38 MAPK, or ERK MAPK pathways (Figure 4C), whereas only JNK inhibition reduced EV-induced p62/SQSTM1 accumulation (Figure 4D). Therefore, JNK signaling is a critical mediator of both barrier dysfunction and autophagy

dysregulation, whereas multiple MAPK pathways are involved in EV-triggered autophagosome formation.

JNK Inhibition Attenuates Barrier Dysfunction and Autophagy in EV-Exposed Human Small Airway Epithelial Cells

EV-induced barrier disruption in hSAEC1-KT was attenuated by pretreatment with a pan-JNK inhibitor (Figure 5A). Confirming that EV induced JNK activation, western blotting and immunofluorescence demonstrated increased phospho-JNK levels (Figure 5, B and C and Supplementary Figure 1C). The EV-triggered accumulation of LC3B-II and p62/SQSTM1 was reduced by JNK inhibition (Figure 5, B, D, and E), indicating improved autophagy completion. EV reduced phospho-S6, indicative of mTOR inhibition regardless of JNK inhibition (Figure 5, F and G), implying that JNK acts downstream or independently of mTOR in regulating the completion of autophagy.

Short-term EV exposure causes persistent cellular stress responses in hamster lungs.

To gain further insights into repair processes and potential long-term consequences of acute EV exposure on lung health, hamsters were exposed to EV aerosols at concentrations shown to simulate human exposure (26) via daily nasal nebulization for 5 consecutive days. To evaluate persistent pulmonary effects of a relatively brief EV aerosol exposure, animals were allowed a 10-day recovery period, with lung tissue harvested on day 15 (Figure 6A). Expectedly, at the time of harvest, EV-exposed and recovered hamsters showed no clinical signs of illness, registered similar body weight changes as those unexposed (Supplementary Figure 2A), confirming that the model of EV exposure was non-toxic. Indeed, histopathological evaluation of the lung parenchyma showed no signs of inflammation or fibrosis (Supplementary Figure 2, B-C). To determine whether the data from human distal lung cells are recapitulated in the animal model, we investigated p62/SQSTM1 accumulation by immunofluorescence microscopy. EV-

exposed animals showed a 4-fold increase in p62 abundance in the distal lung parenchyma, an increase in abundance of p62 colocalizing with CD31-positive endothelial cells lining small pulmonary arteries, and a significant increase in p62 in epithelial cells lining small airways (Figure 6B and C). This suggested a decrease in completion of apoptosis, which would be consistent with decreased overall injury repair. We next evaluated the lung parenchyma for apoptosis, noting that cleaved caspase-3 was present in EV-exposed lungs, even at 10 days post-exposure (Figure 6D). CO-staining for CD31, an endothelial cell marker, and TUNEL (Terminal deoxynucleotidyl transferase dUTP nick end labeling) revealed that endothelial cells had DNA strand breaks at 10 days for-EV exposure (Figure 6E). Taken together, these results suggest modest persistent apoptosis in distal lungs following EV exposure.

Persistent transcriptomic responses in hamster lungs following brief EV exposures

To comprehensively profile biological processes, signaling mechanisms, and disease associations driven by EV exposure, we performed RNA sequencing (RNA-seq) of hamster lungs and subsequently analyzed pathway enrichment. RNAseq, filtered for log2 fold change (FC) >1 or <-1 and $p<0.05$, revealed ~200 upregulated and ~300 downregulated lung genes. In this analysis, while many genes achieved p-value significance, many fewer met the more stringent FDR (q) threshold, likely due to brief nontoxic level of exposure followed by recovery, the inherent variability in transcriptomic data, and the relatively low number of animals per group. However, the observed nominal significance of differentially expressed genes (DEG) may provide biologically meaningful information that will require further corroboration.

To validate the results obtained in human cells, we first interrogated the JNK signaling pathway. Although this was not the top differentially regulated pathway during the recovery from acute EV exposure, interactive pathway analysis predicted that EV activates the JNK signaling pathway due to (nominally) significant increase in expression of upstream JNK activators *Spag9*

(JNK-interacting protein-4; - 4-fold; p=0.03) and *Aida* (Axin Interacting Protein-1; - 9-fold; p=0.02) (Figure 7, A-C), as well as the downstream JNK mediator, *JunD,* which was also increased 5-fold (p=0.003). In addition to JunD, a central signaling pathway hub linking cellular stress to barrier function and autophagy, other notable effector changes were the decrease in *Dach1* (Dachshund Homolog 1), predicted to impair autophagy completion (27) and trigger lung epithelial cell apoptosis, promoting fibrosis(28). EV decreased *Dach1* by 50% (p=0.0007) while upregulating *Ager* (Advanced Glycation End-Product Receptor) and *Eng* (Endoglin), *IL1β, Itgb4* (Integrin B4), and *Tlr4*, which may link EV-induced JNK activation to barrier dysfunction and autophagy. These complementary results demonstrate cross-validation between the human cell experiments and the animal model, reinforcing the biological significance of the identified pathways.

Next, we determined which transcripts are most differentially modified by remote EV exposure in hamster lungs. The top 20 transcripts that were most increased by prior EV exposure in hamster lungs and that reached nominal statistical significance (**Table 1A**) included genes involved in protein degradation (such as ~40-fold increase in Ubiquitin Conjugating Enzyme E2 O), innate immune defense (~14-fold increase in BPI Fold Containing Family B Member 1), coagulation and inflammation (such as ~13-fold increase in tissue factor), cell adhesion and proliferation (such as Tumor-associated calcium signal transducer 2 ad LY6/PlaurDomain Containing 2), and stress response (Sumo1/Sentrin Peptidase 1, Nudix Hydrolase 13, and JunD). The 20 transcripts most decreased by prior EV exposure in hamster lungs, and that reached nominal statistical significance (**Table 2**) were also genes involved primarily in proteostasis and matrix remodeling, such as Ubiquitin Conjugating Enzyme E2 D1, Protease, Serine 35, and Osteopontin, with *Ubl5* (Ubiquitin-like protein 5) registering a statistically significant decrease of > 600-fold (p=4.51E-05, q=0.04). Also downregulated were genes involved in mitochondrial function and the immune response, such as Galectin-9, Cxcr2,

and Nod2. These findings suggest that the EV contributes to a persistent stress response and signaling that impact immune function and tissue remodeling.

Using pathway analysis, when examined by enrichment scores, the top five functional categories of gene pathways impacted by EV (Figure 7D) included Cellular Movement, the most statistically significant function, with 84 genes involved, followed by the Cellular Assembly and Organization pathway with 70 genes, suggesting an important effect on cytoskeletal remodeling, which could impact barrier function, as well as cell migration, and chemotaxis. Cell Death and Survival, Cellular Development, and Cellular Function and Maintenance were also among the top 5 affected functions, reflecting EV-triggered activation of autophagy, stress adaptive survival, and cellular repair mechanisms, with several pathways linked to JNK activation and p62/SQSTM1 accumulation.

When analyzed using patterns related to biological responses or disease associations, pathway enrichment analysis revealed significant activation of Actin Cytoskeleton-, Hepatic Fibrosis-, and Neutrophil Extracellular Trap Signaling (Supplementary Fig. 3A), as well as Cancer, Inflammatory Disease, and Cell-Mediated Immune Response (Supplementary Fig. 3B). Interestingly, gene expression was predominantly inhibited in NET, RHOGDI, and Th1 pathways, suggesting immune suppression or impaired inflammatory resolution. Other activated pathways were linked to metabolism and endocrine regulation, with notable enrichment of the P2Y Purinergic Receptor Signaling, given its key role in airway inflammation, mucus hypersecretion, vascular reactivity, and pulmonary surfactant homeostasis.

Short-term EV exposure alters host lung responses to acute respiratory viral infections in hamster lungs

The transcriptional changes in immune response pathways indicate that EV may modulate host responses to respiratory viral infections. We designed the experiments to

address the following two questions: Does EV pre-exposure modify the lung injury response to SARS-CoV-2? and Does EV pre-exposure modify the effect of co-viral infection (with IAV) on the lung injury induced by SARS-CoV-2? The goal was not to evaluate (the effect of EV on) IAV-induced acute lung injury; rather, IAV served solely as a co-infection with SARS-CoV-2, reflecting a common clinical scenario. Given our focus on SARS-CoV-2–mediated injury, we selected a literature-supported time point corresponding to peak SARS-CoV-2 lung injury, and we exposed hamsters to daily EV for 5 days, followed by SARS-COV-2 (3 days later); or, sequentially, to both IAV (the following day) and SARS-COV-2 (3 days later) (Figure 8A). Lungs were harvested on day 7 after SARS-CoV-2 infection (during the injury phase). This experimental design also enabled us to test the effect of IAV pre-infection on host responses to SARS-CoV-2, with or without EV exposure.

To test the effect of EV on upper airway virus infectivity, we measured oropharyngeal SARS-COV-2 viral titers during the first 3 days following infection (Figure 8B). A 3-way ANOVA factoring time, EV exposure, and IAV infection showed that time ($p=0.004$) played a significant role, and that EV significantly increased viral titers of SARS-COV-2 ($p=0.04$), (Figure 8B). Although IAV infection reduced SARS-COV-2 titers, this did not reach statistical significance in this analysis ($p=0.13$). As expected, at 7 days following SARS-COV-2, animals had significant weight loss that was more pronounced in male animals (Supplementary Figure 2B). EV pre-exposure significantly ($p=0.04$) worsened weight loss in female animals infected with SARS-COV-2 (Figure 8C), while males pre-exposed to EV had less weight loss ($p<0.0001$), (Figure 8C). A 3-way ANOVA factoring EV exposure, IAV co-infection, and sex, showed that IAV and sex had a significant impact on SARS-COV-2 -induced weight loss ($p=0.004$) - with IAV attenuating and male sex accentuating the SARS-COV-2 -induced weight loss -, and that EV significantly interacted with these two variables ($p=0.0006$), modifying their effect on weight loss (Supplementary Figure 2B).

Quantitative analysis of inflammatory cells in the BALF revealed that SARS-CoV-2 infection significantly decreased the abundance of macrophages and increased that of lymphocytes, neutrophils, and eosinophils (Figure 8D, E, H, I). EV preexposure decreased BALF macrophage abundance ($p = 0.01$) and increased lymphocyte abundance ($P = 0.04$) only in female animals co-infected with IAV and SARS-CoV-2 (Figure 8E, G). A 3-way ANOVA factoring EV exposure, sex, and IAV co-infection showed a significant effect of IAV on (increasing) lymphocyte predominance and (decreasing) neutrophil predominance in response to SARS-COV-2 ($p < 0.05$ for each), (Supplementary Figure 2 D, E) - consistent with interference- and confirmed the significant interaction of EV with sex and with sex and IAV on macrophage abundance ($p<0.05$ for each, Supplementary Figure 2C).

Histological analysis of the lungs was consistent with increased inflammatory injury induced by SARS-CoV-2 compared with uninfected lungs, regardless of EV exposure (Figure 8J, K). A 3-way ANOVA factoring EV exposure, sex, and IAV co-infection showed only a trend of impact of EV ($p=0.09$) and sex ($p=0.07$) on lung injury induced by SARS-CoV-2 (Supplementary Figure 2 G).

Overall, these results show that remote short-term exposure to EV is sufficient to alter the susceptibility to respiratory infection with SARS-CoV-2, as evidenced by increased viral titers and weight loss, the latter in a sex-dimorphic fashion. However, these changes were insufficient to cause marked alterations in lung inflammation and injury in response to SARS-CoV-2. Our data also indicate that 3 days of pre-infection with IAV was sufficient to interfere with SARS-CoV-2 infection, reducing its infectivity and its detrimental effect on weight loss, preventing the decrease in, and even increasing, macrophage abundance, increasing lymphocytes, and decreasing eosinophils. EV was synergistic with IAV in its effects on body weight and macrophage and lymphocyte inflammation in females, suggesting in may share mechanistic features of viral interference.

EV exposure changes transcriptome responses to respiratory viral infections

To gain insight into the potential mechanisms underlying anti-viral host responses triggered by EV, the transcriptomic profiles of lungs pre-exposed to EV and then infected with SARS-CoV-2 were compared with those of animals infected but unexposed to EV. Several significant effects were noted (Table 3), including EV-increases in *Mmp13* (3-fold, p= 9.0E-07, q=0.001), *Mmp12* (3-fold, p=0.0001, q=0.035), *Osteopontin* (*Spp1*, 2-fold, p= 0.0002, q=0.05) that, coupled with downregulation of *Timp1* and *Fmod,* suggested EV enhances lung tissue remodeling following virus infection. Downregulation of *Slc31a1* is essential for cytochrome c oxidase (by 30%, p=4.2E-14, q=3.87E-10) and for critical components of the electron transport chain, indicating significant effects on mitochondrial responses to viral infection. EV pre-exposed lungs responded to SARS-CoV-2 with significantly increased neuritin (*NRN1*, 4-fold, p=9.26E-05, q=0.033) a pro-angiogenic molecule with neuroendocrine signaling effects, and decreased TMF-regulated nuclear protein 1 (*TRNP1*, by 80%, p=2.7E-10), an inhibitor of cell proliferation. Pathway analysis showed that lungs pre-exposed to EV exhibited decreased phagosome formation, decreased immune cell death, and enhanced NETosis, IL-12 signaling, muscle cell death, and vascular lesion formation in response to SARS-CoV-2 infection (Figure 10A). When EV preceded both IAV and SARS-CoV-2 infections, similar patterns of differential gene expression were observed, with EV-exposed lungs showing upregulation of genes critical for extracellular matrix integrity and downregulation of genes involved in energy production and protein synthesis (Table 4).

Pathway analyses indicated activation of fibrosis and actin cytoskeletal reorganization (Supplementary Fig 4A), downregulation of antiviral genes and innate immune responses, as well as those involved in immune recruitment and resolution mechanisms (Supplementary Fig. 4B). IL-12 signaling, a central TH1 Immune cytokine that stimulates IFN production and IL-23 and TH17 cell responses, was increased by EV in doubly infected lungs (Supplementary Fig 4C

and D). Overall, these changes suggest that EV exposures are favorable for viral persistence and may promote chronic inflammation in response to viral infections.

IAV pre-infection altered the transcriptional responses to SARS-COV-2 infection, enhancing pulmonary and hepatic fibrosis pathways (Supplementary Figure 5A), increasing estrogen receptor signaling (Supplementary Figure 5A and D), suppressing interferon signaling (Supplementary Figure 5B and C) and cell proliferation, while increasing DNA damage and inhibiting coronavirus pathogenesis pathways (Supplementary Figure 5B).

Discussion

These results indicate that even short-term EV exposure has detrimental effects on lung health, with EVs potentially directly injuring distal lung cells, triggering a stress response that decreases the barrier function of small airway epithelial and lung microvascular endothelial cells, and leading to incomplete cell repair via stress-autophagy that may culminate in apoptosis. This stress response persists for at least 10 days after short-term EV exposures, with transcriptomic changes that predict decreased immune defenses against respiratory viruses, and notable alterations in proteostasis and tissue remodeling that might herald the development of chronic lung diseases following habitual EV use.

The pulmonary consequences of vaping remain an important public health concern marked by important knowledge gaps and the misconception that EV is a safer alternative to cigarette smoking. By focusing on the distal lung, our study addresses unmet needs (29), complementing knowledge of the harmful effects of EV on the proximal airways (30-32) or on specific cell populations (33). By using a popular commercial EV product and integrating studies of human distal lung structural cells with those in laboratory animals that share distal lung anatomy and

immune responses to respiratory virus infection with humans, our study has clinical relevance. However, we did not dissect nicotine-dependent versus nicotine-independent effects, which may be distinct, as shown in previous studies (11, 12, 34-36), nor did we determine the effects of various flavorings, which may have additional effects on the distal lung. Furthermore, due to limitations of BSL-3 regulations at the time of the study, we relied on aerosolizing EV from condensate, which does not retain short-lived volatile compounds such as aldehydes.

Acute EV exposure of both human lung endothelial and epithelial cells disrupted the distal lung structural cell barrier function, thereby weakening lung defenses and promoting inflammation. A hallmark of acute lung injury, several chronic lung diseases, including COPD and lung fibrosis, are also characterized by decreased lung barrier function. We have previously shown that EV decreases lung microvascular endothelial cell barrier function (11), with current results adding mechanistic insight as well as showing, for the first time to our knowledge, a similar permeability increase in small airway epithelial cells grown either at air-liquid interface or submerged, exposed to all forms of EV experimental formulation as vapor, juice, or condensate.

Both cell types underwent autophagy, with accumulation of p62/SQSTM1, suggesting incomplete autophagolysosomal degradation and inefficient repair, as further indicated by increased apoptosis rates in EV-exposed cells. There is ample evidence that stress-induced autophagy is coupled with decreased cell proliferation rates to enable cell survival and repair (37). However, autophagy can directly precede and trigger apoptosis if stress levels are excessive and persistent, or if autophagy is impaired and/or decoupled from other cell repair processes (38). Acute EV exposures induced enrichment of ceramide in the plasma membrane and nuclear translocation of caspase-3, events that have been shown to signify apoptosis (39-41) (42-44). Although the levels of EV exposure studied did not induce massive apoptosis, and apoptotic markers were recorded many hours after the loss of barrier function, it is possible that

apoptosis could, in turn, affect and worsen the barrier function of both the microvascular endothelium and the small airway epithelium. Apoptosis was also modest during recovery from EV exposure in hamster lungs and was primarily found in the distal lungs, where, in addition to cleaved caspase-3 detected in the lung parenchyma, we observed TUNEL staining that colocalized with lung endothelial cells.

Our study implicated JNK, a key mediator of stress-induced autophagy and apoptosis, as a key signaling event to both EV-induced barrier dysfunction and EV-induced autophagy with accumulation of p62/SQSTM1. Other MAPKs activated by stress, such as p38 MAPK (45) have been implicated in the effects of EV in neutrophils (46), but not rat lung microvascular endothelial barrier dysfunction (11). In previous studies, we identified both p38 and JNK as mediators of cigarette smoke-induced cytoskeletal changes in lung endothelial cells, but unlike EV, neither was necessary for barrier dysfunction (47). Interestingly, JNK inhibition did not affect S6 phosphorylation, suggesting the presence of additional mechanisms of mTOR signaling during EV exposure.

As expected from previous reports (31, 48), short-term EV exposures in hamsters, as in mice, and especially when followed by a recovery window, are insufficient to trigger appreciable systemic or lung histopathological changes. However, we designed our experiments to identify lung responses involving cytoskeletal dynamics, inflammation, and metabolic and immune dysregulation that persist even after relatively modest EV exposures. Our data builds on findings recently published by Hinds et al.(24) on 2-day whole-body nicotine solution exposure in hamsters, with immediate histological assessment and targeted gene transcription showing increases in inflammation-related genes IL1β, ELANE (NETosis gene), tissue factor, and pro-fibrotic genes. Our study complements these results by capturing previously unreported persistent effects of acute EV exposures and by providing a much broader transcriptomic

assessment, which shows that IL6 elevations (2.2-fold, p=0.01) and IL1β reductions (by 50%, p=0.01) persist even after EV cessation. In addition, our study shows that EV induces persistent changes in Cytoskeletal Dynamics and Cell Death and Survival pathways, suggesting that EV amplifies inflammation, promotes tissue remodeling, and impairs immune function. Repeated activation of these pathways could therefore lead to persistent airway and vascular remodeling observed in chronic lung diseases. Our study of transcriptomic pathway analysis following sequential EV, IAV, and/or SARS-CoV-2 exposures suggests that EV has a detrimental effect on the lung's ability to respond to SARS-CoV-2 infection, driven by a complex interplay between antiviral immune suppression, augmented tissue remodeling, and mitochondrial dysfunction signaling. Although not a focus of our study, IAV pre-infection had an overall protective, anti-inflammatory priming effect on subsequent SARS-CoV-2 infection. In contrast, EV exerted a detrimental priming effect on respiratory viral infections, leading to exaggerated inflammatory and tissue remodeling responses and impaired injury resolution. We noted a statistically significant interaction between EV effects and animal sex. Although previous studies have shown that sexes may have different susceptibilities to environmental insults, we did not explore the mechanistic underpinnings of our observations. Given the small number of animals in each sex subgroup, these findings will need to be validated in future studies. focusing only on the effect of EV on SARS-CoV-2-induced injury. Another limitation of the in vivo study was that it did not investigate the effect of EVs on IAV-induced lung injury or recovery, as this topic has recently been explored. Instead, we used IAV to model a co-infection with SARS-CoV-2, a common clinical scenario (49, 50). However, pre-administration of IAV at a sublethal dose led to a priming effect, also known as interference (51). Our results could inform future experimental design to fine-tune the timing of IAV co-infection with SARS-CoV-2 to avoid interference. We also acknowledge that validating the sex-specific differences observed in the hamster study with human specimens is necessary in future studies.

In conclusion, this study finds that even short-term EV exposure activates stress responses, induces cell injury, and reduces repair in human cells isolated from the lung parenchyma. It further demonstrates that these changes persist after EV exposure and that even brief EV exposures decrease antiviral immunity, increasing susceptibility to SARS-CoV-2 and influenza virus infections while triggering molecular pathways involved in lung tissue remodeling. The identification of JNK signaling as a modifiable pathway may guide future research on therapeutic strategies to mitigate EV-induced lung injury. These findings provide mechanistic evidence linking EV exposure to impaired lung defense and distal lung remodeling, such as lung fibrosis, informing risk assessments of EV safety and prevention measures against respiratory virus exposures in habitual EV users.

Methods

Sex as a biological variable. Both sexes are included in human cell-based and animal studies. When available, equal incorporation of both sexes in the study design and interpretation.

Study approvals: The studies were performed in line with the principles of the Declaration of Helsinki. This study uses human biological samples from deidentified individuals and was deemed IRB exempt. All studies were conducted under approvals by the institutional IACUC (#1372) at Colorado State University and National Jewish Health and IBC (20-029B) protocols.

Reagents: All reagents were purchased from Sigma-Aldrich/EMD Millipore (St. Louis, MO) unless otherwise stated.

Cell cultures: All cell cultures were maintained in sterile conditions at 37°C and 5% CO2. Primary human lung microvascular endothelial cells (HLMVEC) were obtained from Lonza (Morrisville, NC, CC-2527) and maintained in their appropriate media with standard growth factor supplements (Lonza). Immortalized human lung microvascular endothelial cells (HULEC, ATCC, CRL-3244) were grown in MCDB131 (Corning, 45001-112) media and used in submerged culture. h-TERT-immortalized human small airway epithelial cells (hSAEC1-kt, ATCC, Manassas, VA, CRL 4050) were grown in Pneumacult-Ex Plus Medium (Stemcell Technologies, #05040), characterized for full differentiation at air-liquid interface (Supplementary Figure 6), and used in experiments at earlier stages of differentiation, while submerged in media. Primary human small airway epithelial cells (SAEC) were isolated from the lungs of de-identified organ donors who had not been used for transplantation and whose lungs were donated for medical research. The lung was obtained from the National Jewish Health Human Lung Tissue Core, which obtains deidentified lungs through the National Disease Research Interchange (Philadelphia, PA), the International Institute for the Advancement of Medicine (Edison, NJ), or the Donor Alliance of Colorado. The Committee for the Protection of Human Subjects at National Jewish Health, Denver, CO, deemed this research as IRB human research exempt. Donors were selected without a history of lung disease, lifelong non-smokers, and with the absence of lung injury as indicated by a PaO_2/FiO_2 >300, a chest radiograph that indicated no acute process, and a time on the ventilator of <5 days. Small airway (≤2 mm diameter) epithelial cells were collected from the distal lung using a 2 mm bronchoscopy brush (Conmed, Greenwood Village, CO) and placed in sterile PBS. Cells were isolated by centrifugation, resuspended in PBS, counted, and plated onto an irradiated NIH 3T3 fibroblast feeder layer in F-media. Once visible colonies had formed (7-10 days), they were removed with 0.25% trypsin (Corning, Somerville, MA, 25-053-CI) and plated on double collagen-coated 12-well transwells (Advanced BioMatrix, Carlsbad, CA, 5005 and Corning, 3460). Cells were

maintained in Pneumacult – S-ALI media (StemCell Technologies, Vancouver, Canada, #05001) at 5% CO2 and 37ºC for 21 days.

Human PCLS: Right upper lung lobes from deidentified non-smoking donors with no lung disease or infection were obtained from the International Institute for the Advancement of Medicine (Philadelphia, PA, USA) or the Donor Alliance of Colorado (Denver, CO, USA). Lungs were inflated with 1.5% low-melting agarose (42 °C) and sliced into consecutive sections of 450 µm thickness using a Compresstome® VF-300 vibratome (Precisionary Instruments, Natick, MA, USA). The slices were transferred to 24-well plates containing Dulbecco's Modified Eagle's Medium (DMEM, Thermo Fisher Scientific, Waltham, MA, USA) with antifungal agents and antibiotics and incubated in a humidified incubator at 37 °C, 5% CO_2.

EV exposure of cells: To generate EV, we used Juul pods 5% (59 mg/mL) commercialized as Virginia Tobacco (Juul, San Francisco, CA, USA) with a ratio of 30/70 PG/VG (propylene glycol/ vegetable glycerin). We tested several forms of EV, as juice or aerosol, in submerged and air-liquid interface exposure models, respectively. For submerged cultures, to determine if the vaporized juice has similar effects to the non-vaporized juice on the outcomes tested, we generated EV condensate.

Juul juice was prepared by diluting Juul liquid in serum-free media to a 10x stock solution that was then added to submerged cell cultures or PCLS to achieve a final concentration of 2.5mM - 10mM nicotine. A Vitrocell VC1 apparatus (VITROCELL Systems GMBH, Waldkirch, Germany) was used to generate EV aerosol, which was used to either obtain EV condensate used in submerged cultures, or to directly expose to EV SAEC at the air-liquid interface. The Vitrocell protocol consisted of a modified CORESTA-recommended method # 81, consisting of Puff Volume, 55mL; Puff Duration, 3 Seconds; Puff Frequency, 30 Seconds; Puff hold time 0 Seconds; Puff Exhaust Time, 8 Seconds; Puff Number, 75 puffs. The EV

condensate collected was considered 100% and used at a 5% final concentration in submerged cultures, with ambient air used to generate a control condensate at similar concentrations. For experiments using inhibitors, cells or PCLS were exposed to EV once at the indicated final nicotine concentrations in the presence of absence of: pan-JNK inhibitor (SP600125; 50μM, S1460-10mg, Selleckchem, Houston, TX), ERK1/2 inhibitor (PD98059; 50μM, NC0771630, Fisher Scientific, Hampton, NH), p38-MAPK inhibitor (SB202190; 30μM, S7067-5mg, Sigma), or DMSO as vehicle control.

Cell monolayer barrier measurement was performed using ECIS (Applied Biophysics, Troy, NY) with the Z-Theta 16-well array station. Cell monolayers were grown on 8W10E or 8W10E+ culture ware until a capacitance of < 1 nF or < 10 nF, respectively, at 64 KHz. Measurements of electrical resistance (Ohms) were collected at 4000 Hz over time, which was used to calculate $TER = Net\ Resistance * surface\ area$. A complementary assay to measure the barrier function of cells grown on inserts (0.4 μm x 6.5mm) used fluorescently-labeled dextran (FITC or Rhodamine-B, 4k) applied to the apical side, followed by kinetic measurement of fluorescence in the basal compartment at excitation and emission wavelengths (FITC, Ex 485 Em 538, Rhodamine B, Ex 544 Em 590, respectively).

Immunoblotting: Cells were re-suspended in standard RIPA buffer (R0278, lot # SLBL7395V) on ice for 30 minutes, collected by centrifugation, and quantified using standard BCA assay. Proteins were resolved by 4-20% gradient PAGE and transferred using semi-dry transfer apparatus (Bio-Rad, Hercules, CA) onto Immobilon-P PVDF membranes (IPVH00010; Millipore Sigma, Burlington. MA). Membranes were blocked in Pierce Protein-Free T20 (TBS) Blocking Buffer (Thermo Fisher Scientific, 37571) and washed in TBS with 0.1% Tween-20. Antibodies for immunoblotting were p62 (Abnova, Taipei City, Taiwan, H00008878M01), LC3B-II (Sigma-

Aldrich, L7543), phos-S6 (Cell Signaling Technologies, Danvers, MA, 2211S), anti-vinculin (Abcam, Cambridge, UK, AB130007), or anti-β-actin (Fisher Scientific, Hampton, NH, A5441) and were incubated overnight at 4°C. Anti-mouse (NA931V, lot # 9715064) and anti-rabbit (NA9340V, lot # 10997954) HRP-conjugated secondary antibodies were from GE Healthcare (Chicago, IL).

Cell immunofluorescence microscopy: Human lung endothelial cells or human small airway epithelial cells were plated on chamber slides (Falcon, Culture Slides, #354108) coated with either 12.5µg/mL fibronectin in PBS or 50µg/mL collagen type I in 0.02N glacial acetic acid, respectively. Experiments were conducted on cell monolayers at ~90% confluence. At the end of experiments, cells were fixed in a 4% paraformaldehyde in PBS for 20 minutes at room temperature then permeabilized in 0.5% of Triton-X100 in PBS.

For cell proliferation measurements, cells were incubated with fluorescently labeled synthetic nucleotide, EdU (5-ethynyl-2'-deoxyuridine) dissolved in DMSO (Invitrogen, C10637A) which was added 4 hours prior to experiment completion; briefly, 100X EdU solution in PBS was added to each cell culture for a final EdU concentration of 10µM. The nuclear uptake of EdU was detected using the Invitrogen Click-iT™ Plus EdU Cell Proliferation Kit for Imaging, Alexa Fluor™ 488 dye (Thermofisher, C10637).

For immunofluorescence, following fixation and permeabilization, plated cells were blocked with 5% goat serum and 0.1% Triton-X100 in PBS for 1 hour at room temperature, then incubated overnight at 4°C with primary antibodies, followed by washing and incubation for 4 hours with respective secondary antibodies. This was followed by washing and nuclear staining with DAPI (400ng/mL in of 0.5% bovine serum albumin (BSA) and 0.01% Triton-X100 in PBS) for 20 minutes at room temperature, washing and mounting using ProLong™ Diamond Antifade mounting solution (Invitrogen, P36970). Antibodies were diluted in an antibody buffer consisting of 1% BSA and 0.1% Triton-X100 in PBS. Primary antibodies were against P62 (1:100, mouse

anti-SQSTM1 IgG2a(K), Abnova, H00008878), LC3B (1:100, rabbit anti-LC3B, Sigma, L7543), PCNA (1:200, mouse anti-PCNA IgG2a(K), Novus, NB500-106), Ceramides (1:200, mouse anti-ceramide IgM (MID 15B4), Enzo, ALX-804196-T050), Lamp1 (1:100, rabbit anti-LAMP1 - D2D11- XP®, Cell Signaling Technology, 9091), cleaved caspase-3 (1:200, rabbit anti-cleaved caspase-3, Abcam, ab2302). Primary antibodies were against Mouse IgG2a(K) (1:500, Alexa Fluor™ 594 goat anti-mouse IgG (H+L), Invitrogen, A11032), Mouse IgM (1:500, Alexa Fluor™ 488 goat anti-mouse IgM (μ chain), Invitrogen, A21042), Rabbit IgG (1:500, Alexa Fluor™ Plus 488 goat anti-rabbit IgG (H+L), Invitrogen, A32731 or 1:500 Alexa Fluor™ 647 goat anti-mouse IgG (H+L), Invitrogen, A21245).

Animal Studies. Golden Syrian hamsters (n=6/group, 3 months of age, male, and female; Charles River; Wilmington, MA) were exposed to EV (Juul condensate; 70 puffs/100ul/dose in saline) or vehicle (saline control) via nebulization. Sex as a biological variable was considered in the design (both sexes were included equally) and data analysis and interpretation. EV condensate was collected from the aerosol of vaped Juul in a side-arm Erlenmeyer flask, solubilized in saline, as follows: 7 pods (each 700 μL) were vaporized and the condensate was brought up to 2mL. Each animal was nebulized with EV or vehicle once per day for 5 consecutive days, and lungs were harvested 10 days after the last exposure (Schematic in Figure 6A). The administration of nebulized EV was performed using a nebulizer unit (2.5–4.0 VMD, Aerogen; Galway, Ireland) fitted with a cone that allowed nasal inhalation of the aerosol (5 minutes) by each animal at a time, as we previously reported(11). To assess the effect of EV on respiratory virus infections, hamsters were infected at the end of EV exposure, on day 5, with IAV (influenza virus A; A/California/07/2009) by intranasal instillation of 6 log10 pfu (plaque forming units); and/or, on day 8, with SARS-CoV-2 (WA01), by intranasal instillation of 4 log10 pfu (Schematic in Figure 9A). As controls, uninfected animals were instilled intranasally with 100 μl of PBS or 100 μl of media, respectively. Hamsters were sacrificed 7 days post-SARS-CoV-2

infection. The left lobe was clamped, and the right lung was instilled with PBS (1ml x3) and lavaged, with each return collected separately as bronchoalveolar lavage fluid (BALF) fluid. The first return was used for cytospins. The right caudal lung lobe was excised and placed in Buffer RLT (RNA Lysis Tissue, Qiagen) with freshly added BME (beta-mercaptoethanol). The left lung was inflated with ethanol (70%) and then immersed in formalin (10%), sectioned with a random uniform sampling method, and mounted on cassettes for paraffin embedding.

Lung histochemistry and immunofluorescence:

Cytospins obtained from the BALF were fixed and stained with Diff quick stain using Giemsa Stain (Sigma-Aldrich, GS1L-1L). Samples were fixed to slides using 100% methanol for 10 minutes at room temperature then Giemsa solution (in water) was added for 20 minutes at room temperature. After staining, rinsed slides were air dried and mounted with Cytoseal 60 (Fisher Scientific, 23-244257). Images were taken at 20x magnification. Five hundred cells were assessed for each sample (blinded to the identity of the groups), differentiating among macrophages, lymphocytes, neutrophils and eosinophils by morphological aspect and expressing their abundance as % of all cells counted.

For histological assessment, paraffin-embedded lung sections (4 μm thickness) were stained with hematoxylin and eosin (H&E) and then were assessed unbiasedly (blinded to the animal group identity) under light microscopy using a scoring system for inflammation as originally described (52), and previously applied for models of IAV lung infections (53) and hamster lung inflammation (54). The scoring was applied for each tissue section evaluated, using five criteria: i) the number of bronchioles and bronchi with inflammatory cell infiltrate; ii) the severity of infiltrate of inflammatory cells in bronchioles and bronchi; iii) the severity of bronchiolar and bronchial luminal exudate; iv) the frequency of blood vessels with perivascular inflammatory cell infiltrate; and v) the severity of pneumonia. H&E-stained slides were also

assessed for lung fibrosis using the Ashcroft method, where each microscopic field of the biopsy was assigned an integer score from 0 (normal) to 8 (severe fibrosis).

For TUNEL staining, sections were deparaffinized in xylenes, permeabilized with proteinase K, and post-fixed with 4% paraformaldehyde. They were then washed in PBS, incubated in TdT buffer, then washed with 0.1% triton x-100 in 3% PBS/BSA before being incubated in TUNEL reaction solution. Samples were washed with PBS prior to blocking in PBS/BSA-T. The primary antibody (diluted in PBS/BSA) was added and incubated overnight at 4°C. Samples were washed twice before adding the secondary antibody for 4 hours at room temperature. The samples were washed twice with PBS before being incubated with DAPI and mounted. Images were obtained on an Echo Revolution Microscope (Discover Echo Inc, San Diego, CA).

Bulk RNAseq analyses: Total RNA was isolated using Qiagen All Prep DNA/RNA/Protein kit (Qiagen, Hilden, Germany, #80004). Bulk RNA (RNA Seq) was performed by Novogene (Sacramento, CA) using Illumina RNA-Seq technology. The sequencing data was mapped through STAR software, rMATS (replicate multivariate analysis of transcript splicing), and a ClusterProfiler. The list of differently expressed genes was analyzed with Qiagen's Ingenuity Pathway Analysis (IPA) (Hilden, Germany) using Core Analysis (datasets had a log2 fold change cutoff of ≥ ±1 and p value cutoff of > 0.05) to cross-reference against GO Enrichment and KEGG Analysis results.

Statistical analyses: Analyses of significance were performed using GraphPad Prism 10 software (San Diego, CA). A 2-tailed unpaired Student's t-test was used for experiments in which two conditions were being compared. A P-value < 0.05 was considered statistically significant. Comparisons between groups used ANOVA followed by an intergroup comparison with Tukey's post hoc testing.

For RNAseq analyses, a normalization method of DESeq 2 was utilized, with the fold change being calculated with the equation $[log2(q_{ij}) = \sum_r X_{jr}\beta_{ir}]$. The P-value was calculated using negative binomial distribution $[P(X - x) = (n = x - 1\ n - 1)pn\ (1 - p)x]$ and FDR was calculated using the Benjamini-Hochberg procedure $[FDR = E(FDP(T_{BH})) \leq \frac{T_0}{m,}\alpha\ ]$. Differential Gene Screening was performed with thresholds of |log2(Fold Change) | ≥1 and P-value adjusted ≤ 0.05. Z-Score was calculated through IPA software using $\left[Z = \frac{X}{\sigma_X} = \frac{\Sigma_i W_i X_i}{\sqrt{\Sigma_i W_i^2}}\right]$. Pathways with a z-score ≥ ±2 were considered significant.

Data Availability

Bulk RNA sequencing data generated in this study are available in the Zenodo repository at https://doi.org/10.5281/zenodo.21676278. Of note, the original FASTQ and BAM sequencing files are unavailable for public deposition because the archived files were corrupted and could not be recovered. Supporting data values associated with the main and supplemental figures are provided in the Supporting Data Values Excel file.

Author contributions:

Conceptualization: IP, HWC, RB

Methodology: KSS, RB, EKV, JPP, SDG, GPD, HWC

Investigation: TCR KSS, IP, JP, EVB, SG, RAC, CM, CC, JN

Visualization: NE,

Funding acquisition: IP, HWC

Project administration: IP, RB

Supervision: IP, RB, HWC

Writing – original draft: IP, TCR, KS

Writing – review & editing: IP

TCR assumed leadership of methodology and investigation after KSS relocated. TCR performed all pathway analyses and conducted experiments in SAEC; KSS oversaw the operationalization of the hamster experiment and coordinated with RB and the company performing RNA-seq, which conducted experiments in HLMVEC. They both contributed to writing. Therefore, they share first authorship.

Funding Support

This work is the result of NIH funding, in whole or in part, and is subject to the NIH Public Access Policy. Through acceptance of this federal funding, the NIH has been given the right to make the work publicly available in PubMed Central.

This work was supported by the American Lung Association Grant ALA ETRA736704 (IP); NHLBI grants: R01HL144396 (IP) and HWC; R01HL077328 (IP) and the Wollowick Chair for COPD Research at National Jewish Health (IP).

References

1. Albadrani MS, Tobaiqi MA, Muaddi MA, Eltahir HM, Abdoh ES, Aljohani AM, et al. A global prevalence of electronic nicotine delivery systems (ENDS) use among students: a systematic review and meta-analysis of 4,189,145 subjects. *BMC Public Health.* 2024;24(1):3311.
2. Cooper M, Park-Lee E, Ren C, Cornelius M, Jamal A, and Cullen KA. Notes from the Field: E-cigarette Use Among Middle and High School Students - United States, 2022. *MMWR Morb Mortal Wkly Rep.* 2022;71(40):1283–5.
3. Islam T, Braymiller J, Eckel SP, Liu F, Tackett AP, Rebuli ME, et al. Secondhand nicotine vaping at home and respiratory symptoms in young adults. *Thorax.* 2022;77(7):663–8.
4. McConnell R, Barrington-Trimis JL, Wang K, Urman R, Hong H, Unger J, et al. Electronic Cigarette Use and Respiratory Symptoms in Adolescents. *Am J Respir Crit Care Med.* 2017;195(8):1043–9.
5. Petrache I, Gupta A, Hume PS, Rivera T, Schweitzer KS, and Chu HW. Pathogenesis of E-Cigarette Vaping Product Use-Associated Lung Injury (EVALI). *Compr Physiol.* 2023;13(2):4617–30.
6. Koslow M, and Petrache I. A Finale on EVALI?: The Abated but Not Forgotten Outbreak of Acute Respiratory Illness in Individuals Who Vape. *JAMA Netw Open.* 2020;3(11):e2019366.
7. Carlier FM, de Fays C, and Pilette C. Epithelial Barrier Dysfunction in Chronic Respiratory Diseases. *Front Physiol.* 2021;12:691227.
8. Lu R, Gregory A, Suryadevara R, Xu Z, Jain D, Morrow JD, et al. Lung Transcriptomics Links Emphysema to Barrier Dysfunction and Macrophage Subpopulations. *Am J Respir Crit Care Med.* 2024.
9. Fliesser E, Jandl K, Lins T, Birnhuber A, Valzano F, Kolb D, et al. Lung Fibrosis Is Linked to Increased Endothelial Cell Activation and Dysfunctional Vascular Barrier Integrity. *Am J Respir Cell Mol Biol.* 2024;71(3):318–31.
10. Colunga Biancatelli RML, Solopov P, Dimitropoulou C, Gregory B, Day T, and Catravas JD. The Heat Shock Protein 90 Inhibitor, AT13387, Protects the Alveolo-Capillary Barrier and Prevents HCl-Induced Chronic Lung Injury and Pulmonary Fibrosis. *Cells.* 2022;11(6).
11. Schweitzer KS, Chen SX, Law S, Van Demark M, Poirier C, Justice MJ, et al. Endothelial disruptive proinflammatory effects of nicotine and e-cigarette vapor exposures. *American journal of physiology Lung cellular and molecular physiology.* 2015;309(2):L175–87.
12. Gellatly S, Pavelka N, Crue T, Schweitzer KS, Day BJ, Min E, et al. Nicotine-Free e-Cigarette Vapor Exposure Stimulates IL6 and Mucin Production in Human Primary Small Airway Epithelial Cells. *J Inflamm Res.* 2020;13:175–85.
13. Schaunaman N, Crue T, Cervantes D, Schweitzer K, Robbins H, Day BJ, et al. Electronic cigarette vapor exposure exaggerates the pro-inflammatory response during influenza A viral infection in human distal airway epithelium. *Arch Toxicol.* 2022;96(8):2319–28.
14. Lallai V, Manca L, and Fowler CD. E-cigarette vape and lung ACE2 expression: Implications for coronavirus vulnerability. *Environ Toxicol Pharmacol.* 2021;86:103656.
15. Dhanasekaran DN, and Reddy EP. JNK-signaling: A multiplexing hub in programmed cell death. *Genes Cancer.* 2017;8(9-10):682–94.

16. Sui X, Kong N, Ye L, Han W, Zhou J, Zhang Q, et al. p38 and JNK MAPK pathways control the balance of apoptosis and autophagy in response to chemotherapeutic agents. *Cancer Lett.* 2014;344(2):174–9.
17. Liu S, Yao S, Yang H, Liu S, and Wang Y. Autophagy: Regulator of cell death. *Cell Death Dis.* 2023;14(10):648.
18. Kanamori K, Ahmad SM, Hamid A, and Lutfy K. Chronic Exposure to E-Cigarettes Elevates CYP2A5 Activity, Protein Expression, and Cotinine-Induced Production of Reactive Oxygen Species in Mice. *Drug Metab Dispos.* 2024;52(3):171–9.
19. Garcia-Arcos I, Geraghty P, Baumlin N, Campos M, Dabo AJ, Jundi B, et al. Chronic electronic cigarette exposure in mice induces features of COPD in a nicotine-dependent manner. *Thorax.* 2016;71(12):1119–29.
20. Madison MC, Landers CT, Gu BH, Chang CY, Tung HY, You R, et al. Electronic cigarettes disrupt lung lipid homeostasis and innate immunity independent of nicotine. *The Journal of clinical investigation.* 2019;129(10):4290–304.
21. Crotty Alexander LE, Drummond CA, Hepokoski M, Mathew D, Moshensky A, Willeford A, et al. Chronic inhalation of e-cigarette vapor containing nicotine disrupts airway barrier function and induces systemic inflammation and multiorgan fibrosis in mice. *Am J Physiol Regul Integr Comp Physiol.* 2018;314(6):R834–R47.
22. Kennedy AR, Desrosiers A, Terzaghi M, and Little JB. Morphometric and histological analysis of the lungs of Syrian golden hamsters. *J Anat.* 1978;125(Pt 3):527–53.
23. Bednash JS, Kagan VE, Englert JA, Farkas D, Tyurina YY, Tyurin VA, et al. Syrian hamsters as a model of lung injury with SARS-CoV-2 infection: Pathologic, physiologic, and detailed molecular profiling. *Transl Res.* 2022;240:1–16.
24. Hinds DM, Nick HJ, Vallin TM, Bloomquist LA, Christeson S, Bratcher PE, et al. Acute vaping in a golden Syrian hamster causes inflammatory response transcriptomic changes. *Am J Physiol Lung Cell Mol Physiol.* 2022;323(5):L525–L35.
25. Ramirez RD, Sheridan S, Girard L, Sato M, Kim Y, Pollack J, et al. Immortalization of human bronchial epithelial cells in the absence of viral oncoproteins. *Cancer research.* 2004;64(24):9027–34.
26. Been T, Traboulsi H, Paoli S, Alakhtar B, Mann KK, Eidelman DH, et al. Differential impact of JUUL flavors on pulmonary immune modulation and oxidative stress responses in male and female mice. *Arch Toxicol.* 2022;96(6):1783–98.
27. Lin J, Li B, Xu Q, Liu YS, Kang YL, Wang X, et al. DACH1 attenuated PA-induced renal tubular injury through TLR4/MyD88/NF-kappaB and TGF-beta/Smad signalling pathway. *J Endocrinol Invest.* 2024;47(6):1531–44.
28. Lu Y, Tang K, Wang S, Tian Z, Fan Y, Li B, et al. Dach1 deficiency drives alveolar epithelium apoptosis in pulmonary fibrosis via modulating C-Jun/Bim activity. *Transl Res.* 2023;257:54–65.
29. Jasper AE, Sapey E, Thickett DR, and Scott A. Understanding potential mechanisms of harm: the drivers of electronic cigarette-induced changes in alveolar macrophages, neutrophils, and lung epithelial cells. *American journal of physiology Lung cellular and molecular physiology.* 2021;321(2):L336–L48.
30. de Lima JM, Macedo CCS, Barbosa GV, Castellano LRC, Hier MP, Alaoui-Jamali MA, et al. E-liquid alters oral epithelial cell function to promote epithelial to mesenchymal transition and invasiveness in preclinical oral squamous cell carcinoma. *Sci Rep.* 2023;13(1):3330.
31. Hwang JH, Lyes M, Sladewski K, Enany S, McEachern E, Mathew DP, et al. Electronic cigarette inhalation alters innate immunity and airway cytokines while increasing the virulence of colonizing bacteria. *J Mol Med (Berl).* 2016;94(6):667–79.

32. Bodas M, Van Westphal C, Carpenter-Thompson R, D KM, and Vij N. Nicotine exposure induces bronchial epithelial cell apoptosis and senescence via ROS mediated autophagy-impairment. *Free Radic Biol Med.* 2016;97:441–53.
33. Scott A, Lugg ST, Aldridge K, Lewis KE, Bowden A, Mahida RY, et al. Pro-inflammatory effects of e-cigarette vapour condensate on human alveolar macrophages. *Thorax.* 2018;73(12):1161–9.
34. Boulay ME, Henry C, Bosse Y, Boulet LP, and Morissette MC. Acute effects of nicotine-free and flavour-free electronic cigarette use on lung functions in healthy and asthmatic individuals. *Respir Res.* 2017;18(1):33.
35. Lechasseur A, Huppe CA, Talbot M, Routhier J, Aubin S, Beaulieu MJ, et al. Exposure to nicotine-free and flavor-free e-cigarette vapors modifies the pulmonary response to tobacco cigarette smoke in female mice. *Am J Physiol Lung Cell Mol Physiol.* 2020;319(4):L717–L27.
36. Wang Q, Lucas JH, Pang C, Zhao R, and Rahman I. Tobacco and menthol flavored nicotine-free electronic cigarettes induced inflammation and dysregulated repair in lung fibroblast and epithelium. *Respir Res.* 2024;25(1):23.
37. Wang RC, and Levine B. Autophagy in cellular growth control. *FEBS Lett.* 2010;584(7):1417–26.
38. Marino G, Niso-Santano M, Baehrecke EH, and Kroemer G. Self-consumption: the interplay of autophagy and apoptosis. *Nat Rev Mol Cell Biol.* 2014;15(2):81–94.
39. Nepali PR, and Haimovitz-Friedman A. Chemotherapeutic Agents-Induced Ceramide-Rich Platforms (CRPs) in Endothelial Cells and Their Modulation. *Methods Mol Biol.* 2021;2187:215–21.
40. Dorweiler TF, Singh A, Ganju A, Lydic TA, Glazer LC, Kolesnick RN, et al. Diabetic retinopathy is a ceramidopathy reversible by anti-ceramide immunotherapy. *Cell metabolism.* 2024;36(7):1521–33 e5.
41. Miyaji M, Jin ZX, Yamaoka S, Amakawa R, Fukuhara S, Sato SB, et al. Role of membrane sphingomyelin and ceramide in platform formation for Fas-mediated apoptosis. *J Exp Med.* 2005;202(2):249–59.
42. Wang Y, Sun L, Xia C, Ye L, and Wang B. P38MAPK regulates caspase-3 by binding to caspase-3 in nucleus of human hepatoma Bel-7402 cells during anti-Fas antibody- and actinomycin D-induced apoptosis. *Biomed Pharmacother.* 2009;63(5):343–50.
43. Kamada S, Kikkawa U, Tsujimoto Y, and Hunter T. Nuclear translocation of caspase-3 is dependent on its proteolytic activation and recognition of a substrate-like protein(s). *The Journal of biological chemistry.* 2005;280(2):857–60.
44. Luo M, Lu Z, Sun H, Yuan K, Zhang Q, Meng S, et al. Nuclear entry of active caspase-3 is facilitated by its p3-recognition-based specific cleavage activity. *Cell Res.* 2010;20(2):211–22.
45. Getiye Y, Peterson MR, Phillips BD, Carrillo D, Bisha B, and He G. E-cigarette exposure with or without heating the e-liquid induces differential remodeling in the lungs and right heart of mice. *J Mol Cell Cardiol.* 2022;168:83–95.
46. Higham A, Rattray NJ, Dewhurst JA, Trivedi DK, Fowler SJ, Goodacre R, et al. Electronic cigarette exposure triggers neutrophil inflammatory responses. *Respir Res.* 2016;17(1):56.
47. Schweitzer KS, Hatoum H, Brown MB, Gupta M, Justice MJ, Beteck B, et al. Mechanisms of lung endothelial barrier disruption induced by cigarette smoke: role of oxidative stress and ceramides. *American journal of physiology Lung cellular and molecular physiology.* 2011;301(6):L836–46.
48. Glynos C, Bibli SI, Katsaounou P, Pavlidou A, Magkou C, Karavana V, et al. Comparison of the effects of e-cigarette vapor with cigarette smoke on lung function and inflammation in mice. *Am J Physiol Lung Cell Mol Physiol.* 2018;315(5):L662–L72.

49. Lansbury L, Lim B, Baskaran V, and Lim WS. Co-infections in people with COVID-19: a systematic review and meta-analysis. *J Infect.* 2020;81(2):266–75.
50. Swets MC, Russell CD, Harrison EM, Docherty AB, Lone N, Girvan M, et al. SARS-CoV-2 co-infection with influenza viruses, respiratory syncytial virus, or adenoviruses. *Lancet.* 2022;399(10334):1463–4.
51. Wu A, Mihaylova VT, Landry ML, and Foxman EF. Interference between rhinovirus and influenza A virus: a clinical data analysis and experimental infection study. *Lancet Microbe.* 2020;1(6):e254–e62.
52. Cimolai N, Taylor GP, Mah D, and Morrison BJ. Definition and application of a histopathological scoring scheme for an animal model of acute Mycoplasma pneumoniae pulmonary infection. *Microbiol Immunol.* 1992;36(5):465–78.
53. Nouri HR, Schaunaman N, Kraft M, Li L, Numata M, and Chu HW. Tollip deficiency exaggerates airway type 2 inflammation in mice exposed to allergen and influenza A virus: role of the ATP/IL-33 signaling axis. *Front Immunol.* 2023;14:1304758.
54. Gally F, Minor MN, Smith SK, Case SR, and Chu HW. Heat shock factor 1 protects against lung mycoplasma pneumoniae infection in mice. *J Innate Immun.* 2012;4(1):59–68.

Figure 1. Barrier function of endothelial and epithelial monolayers following EV-exposure
A,C. Representative tracings of kinetics of rans-endothelial/epithelial electrical resistance (TER), normalized and expressed as fold change vs. initial (prior to exposure), of primary human lung microvascular endothelial cells (HLMVEC, A) and transformed human small airway epithelial cells (hSAEC1-KT, C) exposed to EV at the indicated concentrations. **B**. Scatter plot of normalized TER measured in HLMVEC exposed to EV for 10h. Mean ± SEM; symbols are individual biological replicates; One-way ANOVA with Tukey Test (n=6-28, ****p<0.0001). **D.** Scatter plot of fluorescence intensity, measured in arbitrary units (AU) in the basolateral chamber of apically applied FITC-labeled Dextran (4 kD) to a primary human SAEC pseudostratified layer grown on a transwell to air liquid interface for 21 days and exposed to EV (7.5 mM) for the indicated time. Mean ± SEM; symbols are individual biological replicates; 1-way ANOVA (n=6-29, *p<0.05). UT, untreated; ns, non-statistically significant.

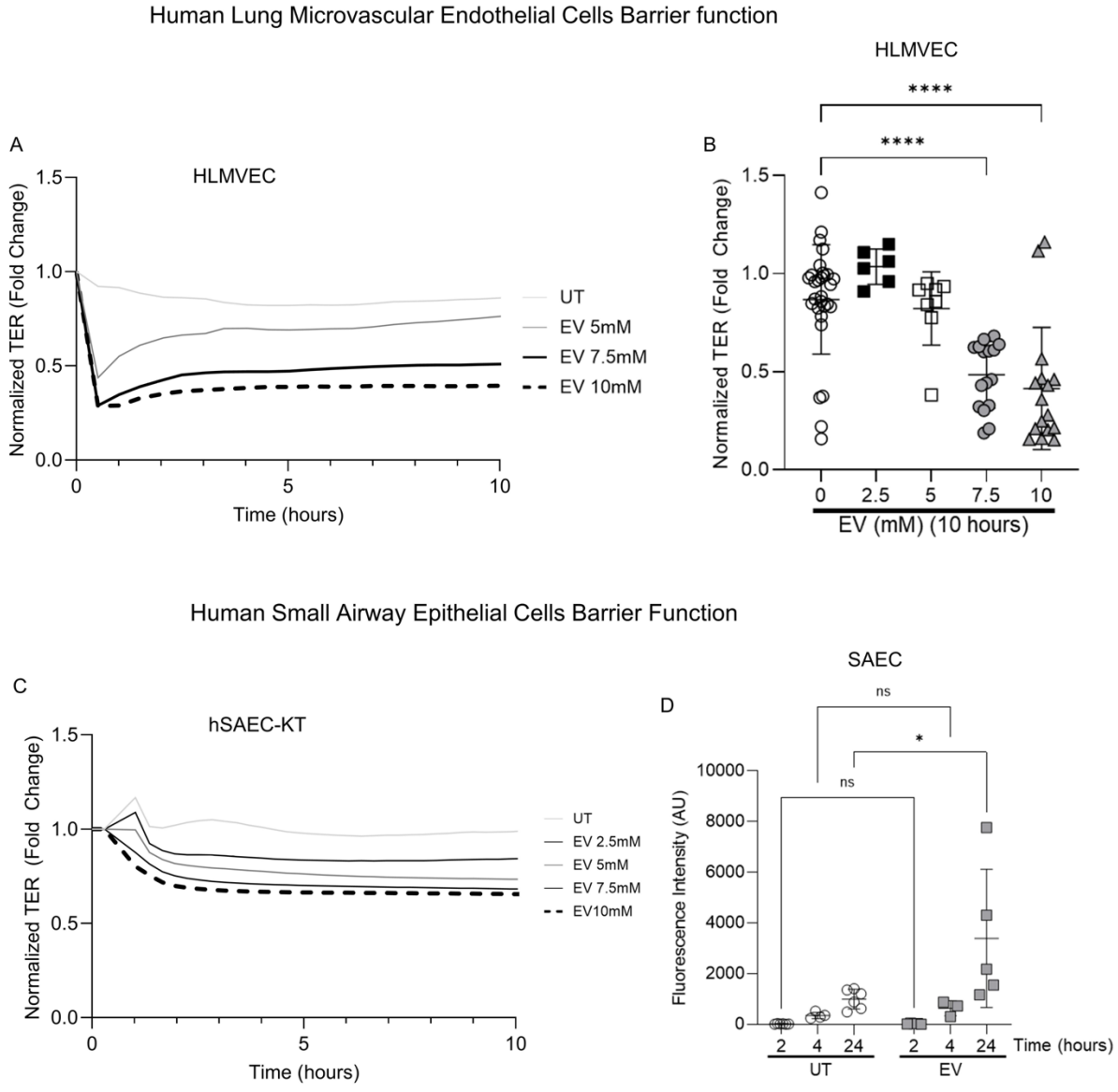

Figure 2. Effect of EV-exposure on human lung microvascular endothelial cell autophagy
A. Representative western blots of LC3B-II, p62/SQSTM1, and phosphorylated S6 in HLMVEC exposed to EV (7.5 mM; 24 hours); **B-D**. Scatter plot of respective protein abundance measured by densitometry and expressed relative to vinculin loading control; Mean ± SEM; symbols are individual biological replicates; unpaired t-test, (B, n=4, p=0.03), (C, n=7, p=0.002), (D, n=5, p=<0.0001). **E-G**. Representative immunofluorescence (IF) image of cells exposed to EV (7.5 mM; 24 hours) and stained for nuclei with DAPI (blue) and for (**E**) incorporated fluorescently labeled EdU (green); (**F**) ceramide (green); or (**F**) cleaved caspase-3 (magenta). UT, untreated. Note that EV-exposed cells showed decreased proliferation; increased ceramide abundance predominantly localized peri-nuclear (solid arrows in inset) and in plasma membrane (interrupted line arrow in inset); and increased cleaved caspase-3 abundance with almost exclusive nuclear localization (inset).

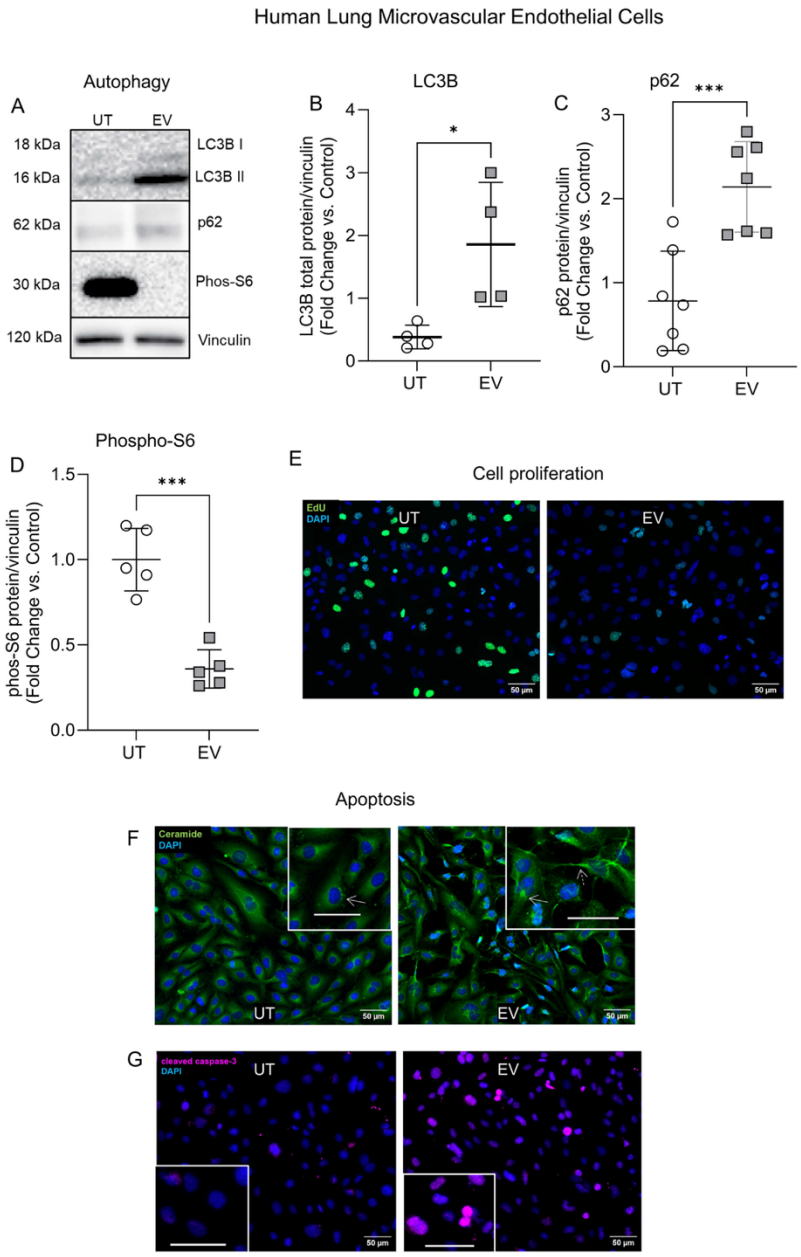

Figure 3. Effect of EV-exposure on human lung small airway epithelial cell autophagy
A. Representative Western blots of LC3B-II and p62 in hSAEC1-KT exposed to EV (7.5 mM; 24 hours); **B-C**. Scatter plot of respective protein abundance measured by densitometry and expressed relative to β-actin loading control; Mean ± SEM; symbols are individual biological replicates; unpaired t-test, (B, n=4, p=.003), (C, n=4, ***p=<0.001). **D**. Representative immunofluorescence microscopy images of hSAEC1-KT exposed to EV (7.5 mM; 24 hours) and stained for nuclei with DAPI (blue) and for (**D**) LC3B (green); (**E**) p62 (red); (**F**) incorporated fluorescently labeled EdU (green); (**G**) ceramides; and (**H**) cleaved PARP (green). **I.** Representative western blots of p62 and cPARP with actin as loading control in hSAEC-KT cells exposed to EV condensate or ambient air condensate (AC); (5%; 24 hours, n=3); UT, untreated.
J. Representative western blots of LC3B-I/II and p62 with vinculin as loading control in human precision cut lung slices exposed to EV at the indicated concentrations (n=5) with relative changes measured by densitometry.

Figure 3

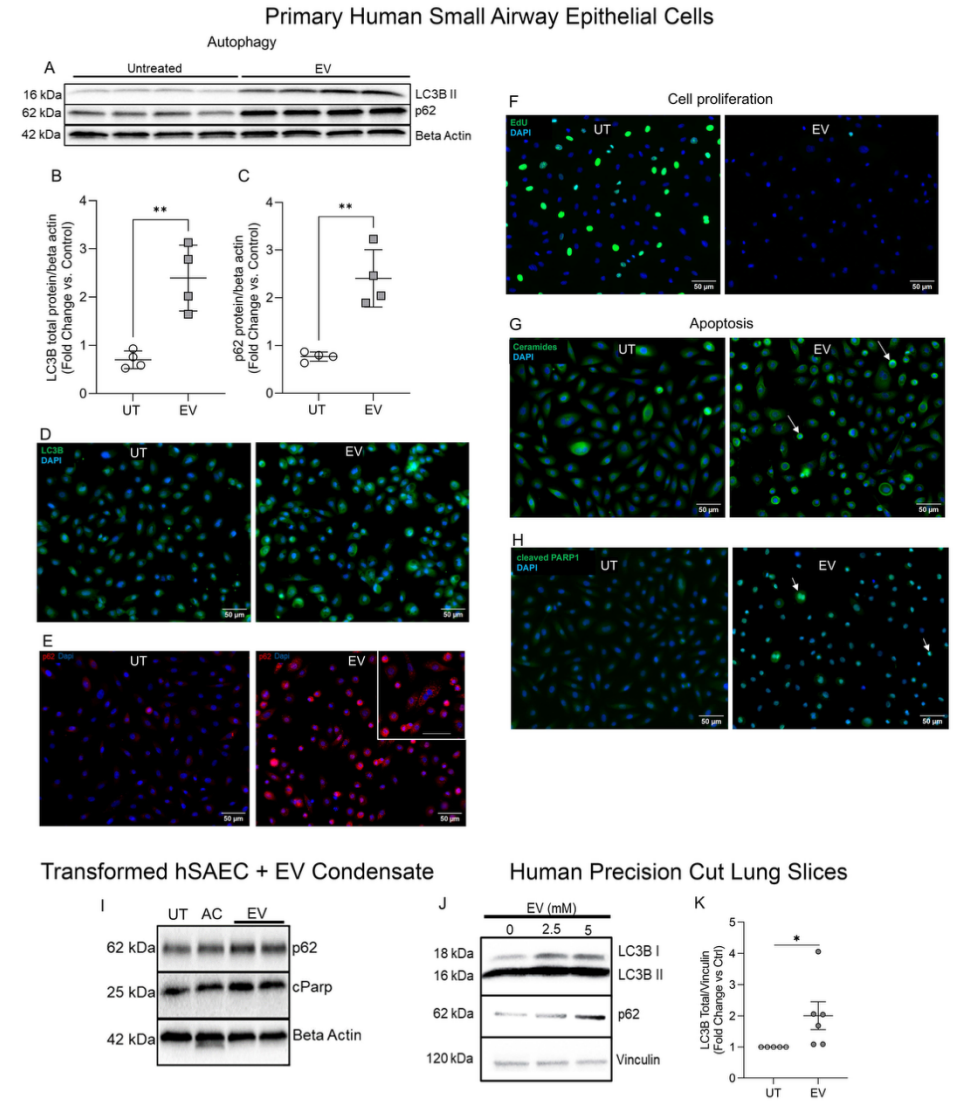

Figure 4. Role of JNK in EV-induced human lung microvascular endothelial autophagy
A. Representative tracings of kinetics of normalized TER, expressed as fold change vs. initial measurement in HLMVEC exposed to EV (7.5mM) in the presence of JNK inhibitor (JNK_{inh}, SP600125; 50μM) or its vehicle (Veh; DMSO; 1%). **B**. Scatter plot of normalized TER measured in HLMVEC exposed to EV (7.5mM; 30 minutes) in the presence of JNK_{inh} or Veh; Mean ± SEM; symbols are individual biological replicates; One-way ANOVA, Tukey Test (n=4-6, ***p=<0.001; ****p=<0.0001). **C-D**. Scatter plot of densitometry of (**C**) LC3B-II and (**D**) p62 relative to vinculin loading control in HLMVEC exposed to EV (7.5mM; 24 hours) in the presence of JNK_{inh}, p38 MAPK inhibitor ($p38_{inh}$; SB202190; 30μM); ERK inhibitor (ERK_{inh}; PD98059; 50μM), or Veh (Mean ± SEM; One-way ANOVA, Tukey Test; C, n=2-11, *p=0.03; D, n=2-22, *p=0.01). Representative western blot of p62 and vinculin shown in D. **E**. Scatter plot of relative abundance of p62 relative to DAPI detected by immunofluorescence (IF) microscopy and measured by blinded automatic image analysis, in HULEC exposed to EV (7.5mM; 24 hours) in the presence of Veh or JNK_{inh} (Mean ± SEM; Two-way ANOVA, Tukey test, n=3, *p<0.05, **p<0.01). **F**. Representative IF images of HULEC exposed to EV in the presence of vehicle (left) or JNK_{inh} (right panel), immuno-stained for p62/SQSTM1 (green), lysosomes (LAMP1, red), and nuclei (DAPI, blue). Yellow arrows indicate superimposed p62 and LAMP1 staining (yellow) suggesting autophago-lysosome fusion events. UT, untreated.

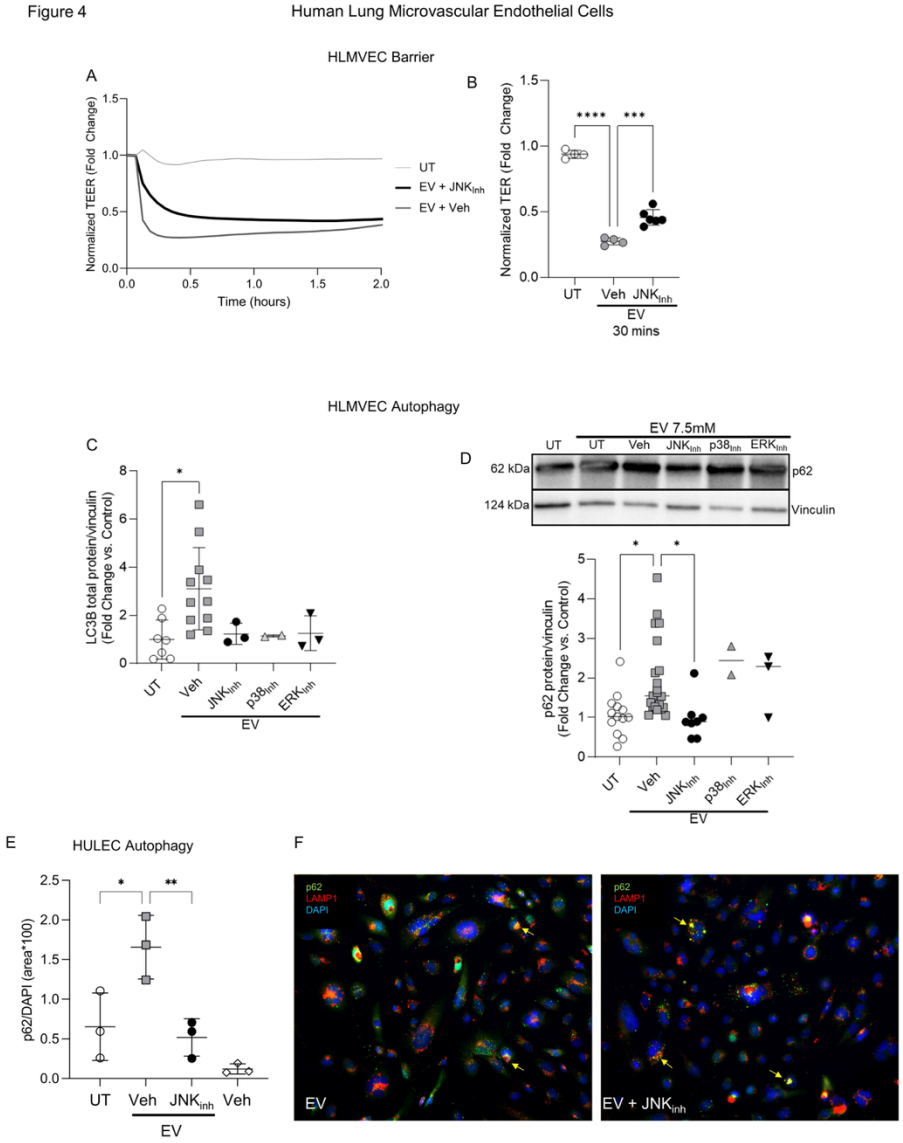

Figure 5. Role of JNK in EV-induced human lung small airway epithelial autophagy

A. Representative tracings of kinetics of TER, normalized and expressed as fold change vs. initial measurement in hSAEC1-KT exposed to EV (5- or 7.5mM) in the presence of JNK_{inh} (SP600125; 50μM) or vehicle (DMSO). **B-E**. Representative western blots (B) and respective densitometries of phospho-JNK (C), LC3B-II (D), and p62 (E) relative to beta actin (as loading control) in hSAEC1-KT exposed to EV (5- or 7.5mM, 24hours) in the presence of JNK_{inh} (SP600125; 50μM) or vehicle. **F-G** Representative western blots (B) and respective densitometries of phospho-S6 relative to beta actin. (C, D, E, G, Mean ± SEM; symbols are individual biological replicates, n=3 in each; One-way ANOVA, Tukey Test, *p<0.05; ** p<0.01; ****p=<0.0001). UT, untreated.

Figure 5

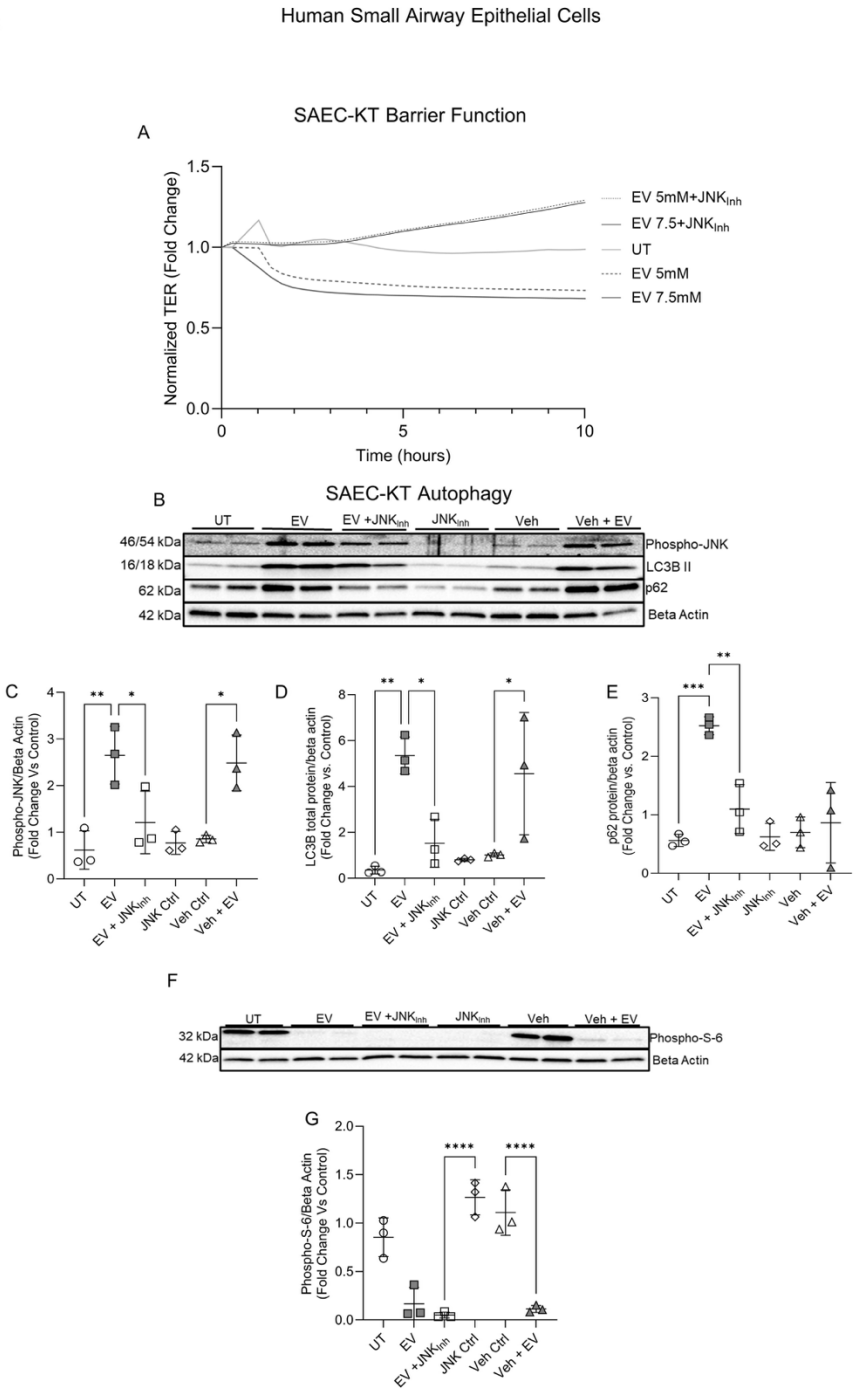

Figure 6. Persistent effects of brief EV exposure on distal lung autophagy in Golden Syrian hamsters

A. Schematic of experimental design depicting daily EV exposure via inhalation for five consecutive days, followed by removal from exposure for 10 days and harvest at day 15. **B**. Representative immunofluorescence images of EV-exposed hamster lung parenchyma stained for nuclei (DAPI, blue), autophagy marker p62/SQSTM1 (green), and endothelial cell marker CD31 (Red). **C**. Respective scatter plots of abundance of p62 in the parenchyma- including endothelial cell colocalization scores (PCC); in the vascular endothelium; and the airway epithelium, as indicated. **D-E**. Representative immunofluorescence images of EV-exposed hamster lung parenchyma stained for nuclei (DAPI, blue) and D. cleaved caspase-3 (red, yellow arrows) or E. DNA strand break marker TUNEL (green, yellow arrows) and endothelial cell marker CD31 (red). Note the colocalization of TUNEL-CD31 in EV-exposed lung parenchyma (magenta arrowheads). As a positive control, lung slides were treated with DNAse.

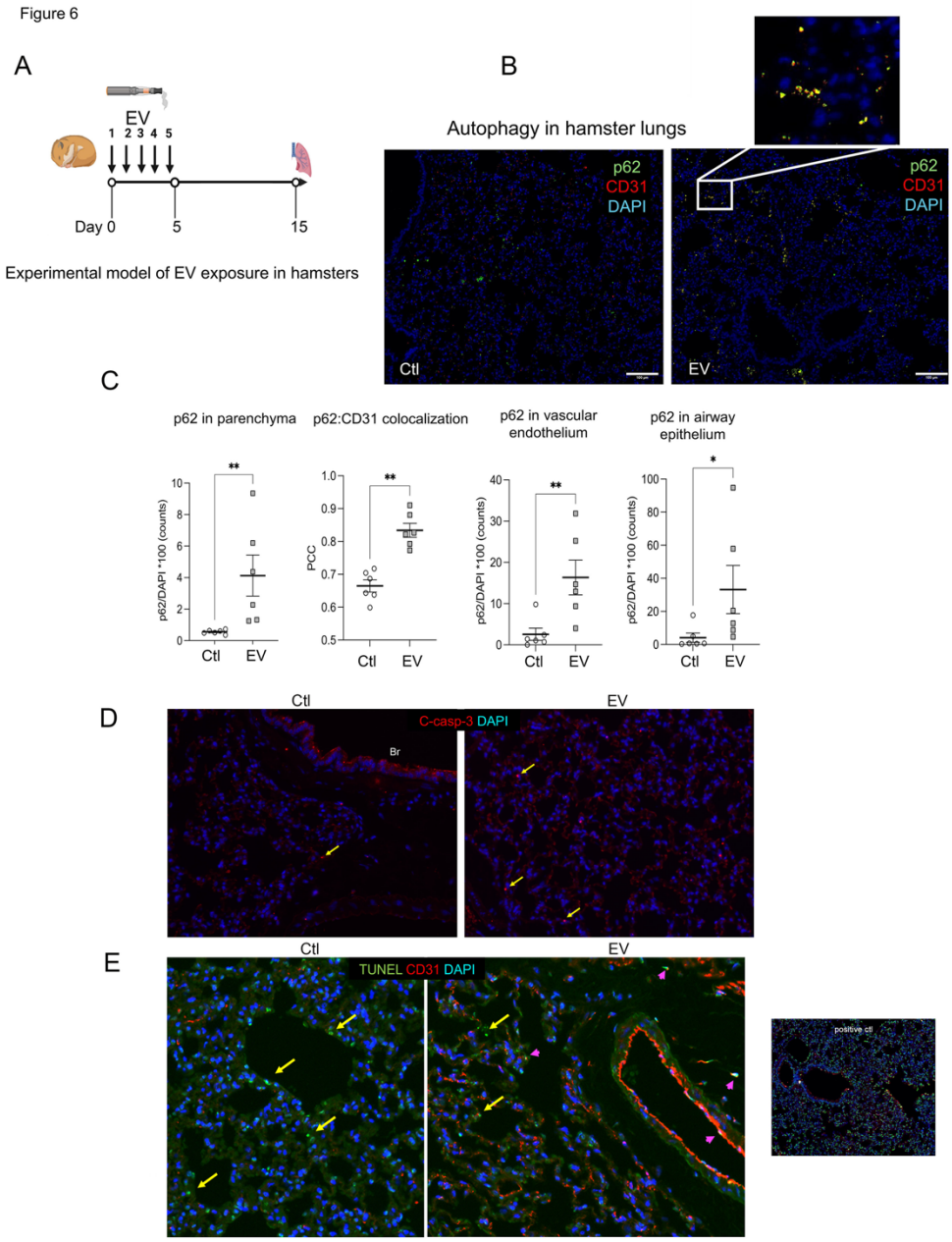

Figure 7. **Interactivity map of JNK signaling induced by brief distant EV exposure in hamster lungs A-C**. Persistent EV effects on JNK-anchored signaling pathways linked to endothelial barrier function (A), epithelial barrier function (B), and cell autophagy (C). Molecules that are predicted or measured as activated are shown in orange or red, respectively (with indicated log 2 fold changes), and those that are predicted or measured to be inhibited are shown in blue or green, respectively. Note predicted JNK activation by upstream regulators (e.g., Spag9, Pkcs, Aida), and downstream activation of JunD, Ap1, and of pro-inflammatory mediators such as IL1B. Jnk is predicted to drive autophagy in epithelial and endothelial cells through pathways involving Tlr4 and Eng, respectively. JunD activation (red), which promotes autophagy via transcriptional activation of Itgb4 and Ager, should lead to mTOR upregulation and subsequent autophagy regulation through Becn1. However, downstream mTOR targets are not increased, suggesting its activity is suppressed. Ager/Tlr4 signaling drives epithelial autophagy, whereas ENG signaling mediates endothelial autophagy. D. Dot plot graph and summary table showing the p-value distribution for pathways involved in cellular and molecular function and the corresponding number of molecules involved.

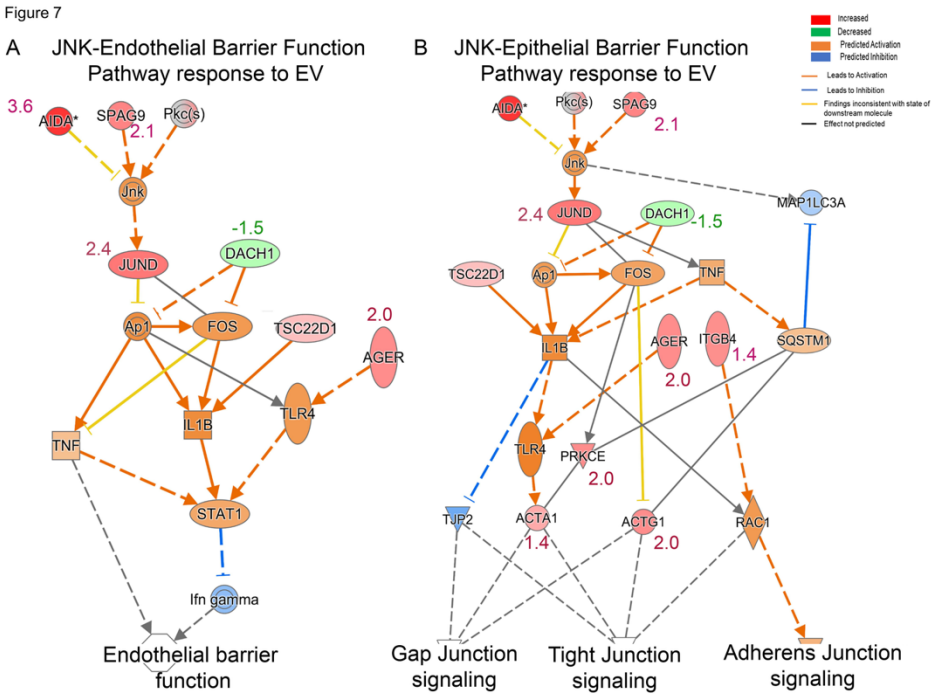

D Cellular function pathways most significantly affected by EV

	p-value range	# Molecules
Cellular Movement	1.67E-03 - 1.98E-07	84
Cellular Assembly and Organization	1.69E-03 - 1.12E-06	70
Cell Death and Survival	1.56E-03 - 6.13E-06	92
Cellular Development	1.20E-03 - 6.96E-06	88
Cellular Function and Maintenance	1.70E-03 - 6.96E-06	103

Figure 8. Effects of brief prior EV exposure on inflammatory responses to respiratory viral infections in hamsters. **A.** Experimental timeline: Exposure to EV for 5 days prior to intranasal administration of influenza A virus (IAV), followed 3 days later by intranasal administration of SARS-CoV-2 (COV2). Viral titers were measured at days 1, 2, and 3 post-infection (dpi) with SARS-CoV-2; lung tissues and BALF were collected at 7 dpi with SARS-CoV-2 (10 days after cessation of EV exposure). **B**. Upper respiratory viral titers obtained by nasal swabs at the indicated time (days) following COV infection. Mean ± SEM. 3-way ANOVA. **C.** Change in body weight in female and male hamsters from pre-infection weight. Mean ± SEM. 2-way ANOVA with Fisher's LSD. **D-I.** Quantification of indicated inflammatory cell population abundance in cytospins of BALF; Mean ± SEM; 2-way ANOVA with Fisher's LSD. **J.** Representative hematoxylin and eosin-stained lung tissue sections from uninfected, SARS-CoV-2, and co-infected (IAV+COV-2) hamsters show exuberant inflammatory infiltrate in SARS-CoV-2-infected lungs. **K.** Unbiased histological scoring of inflammatory lung injury (based on epithelial thickening, inflammatory cell infiltration). Mean ± SEM; 2-way ANOVA with Fisher's LSD. For all graphs, *p<0.05; ** p<0.01; ** p<0.001; ****p=<0.0001; dots are individual animals; UT, untreated.

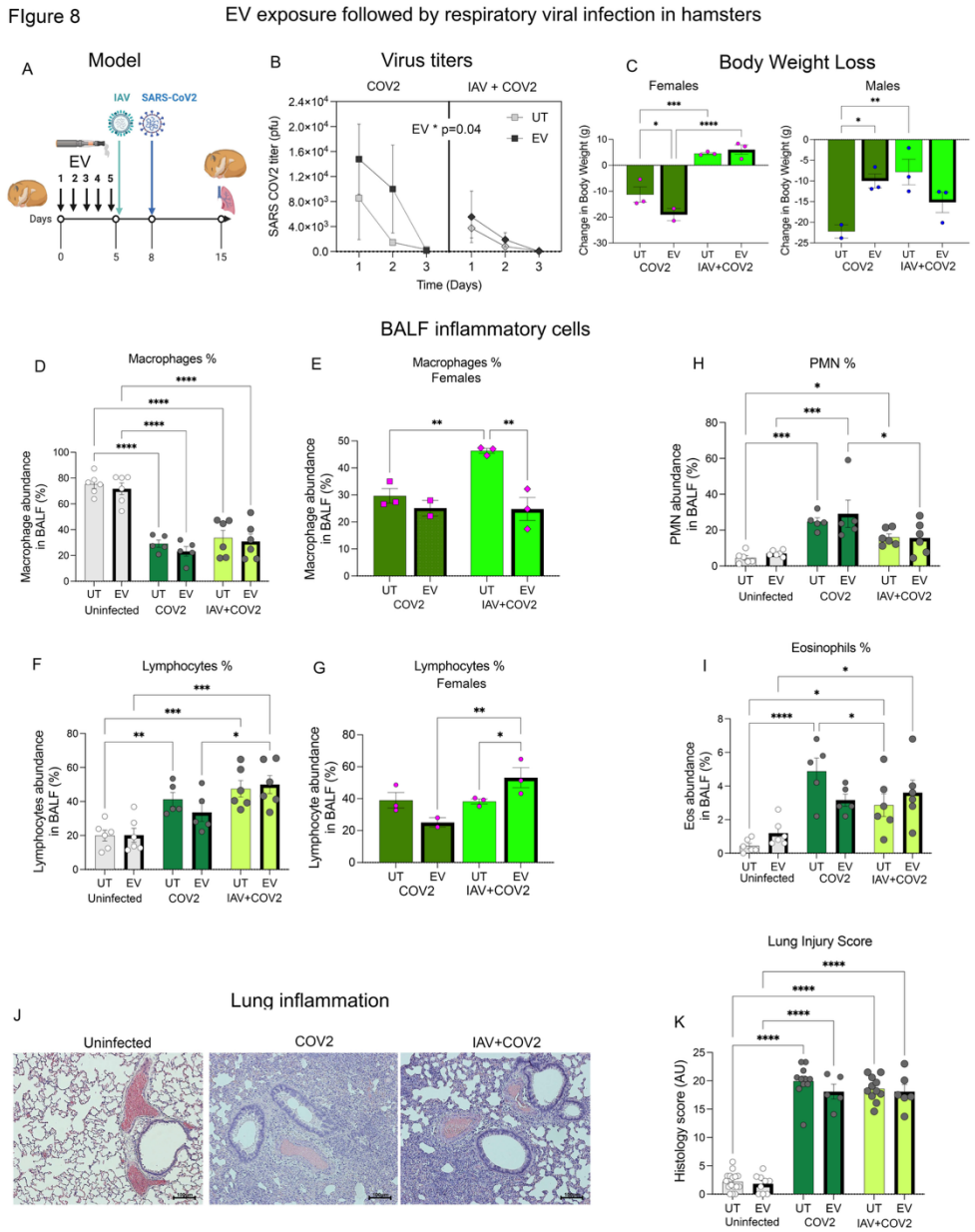

Table 1. Top 20 upregulated genes in hamster lung following EV exposure

Gene	Log2 Fold Change	P-Value	Full Name and Function
Ube2o	4.363	0.00463	Ubiquitin Conjugating Enzyme E2 O - Involved in protein ubiquitination and degradation.
Tacstd2	4.22	0.0009	Tumor-associated calcium signal transducer 2 - Involved in cell adhesion and cancer progre
Bpifb1	3.856	0.0107	BPI Fold Containing Family B Member 1 - Lipid-binding protein involved in innate immunity.
F3	3.711	0.012	Coagulation Factor III (Tissue Factor) - Initiates blood coagulation and promotes inflammation.
Sft2d2	3.629	0.0397	SFT2 Domain Containing Protein 2 - Functions in vesicle trafficking and membrane fusion.
Senp1	3.452	0.0211	SUMO1/Sentrin Peptidase 1 - Regulates de-SUMOylation and protein stress response.
Nudt13	3.304	0.036	Nudix Hydrolase 13 - Involved in nucleotide metabolism and cellular stress responses.
Iqck	3.036	0.0103	IQ Motif Containing K - Putative regulator of calcium signaling pathways.
Mcm9	2.898	0.0205	Minichromosome Maintenance Complex Component 9 - Essential for DNA replication and genome stability.
Gas2l1	2.828	0.0159	Growth Arrest Specific 2 Like 1 - Cytoskeletal protein involved in actin stabilization.
Ckm	2.814	0.0224	Creatine Kinase, Muscle - Key enzyme in energy metabolism and ATP regeneration.
Enpp1	2.778	0.0128	Ectonucleotide Pyrophosphatase/Phosphodiesterase 1 - Regulates extracellular nucleotide levels and mineralization.
Znf365	2.603	0.0103	Zinc Finger Protein 365 - Involved in DNA repair and genomic stability.
Ube2s	2.581	0.0169	Ubiquitin Conjugating Enzyme E2 S - Targets proteins for degradation during cell cycle progression.
Cacnb4	2.541	0.047	Calcium Channel Voltage-Dependent Beta 4 Subunit - Regulates calcium influx in signaling pathways.
Cand2	2.511	0.0291	Cullin-associated NEDD8-dissociated protein 2 - Implicated in muscle contraction and signaling pathways.
Fam189a2	2.442	0.0217	Family with Sequence Similarity 189 Member A2 - A membrane protein linked to signal transduction.
Jund	2.41	0.00033	Jun D Proto-Oncogene - Component of the AP-1 transcription factor, regulates stress and inflammation.
Lypd2	2.389	0.0108	LY6/PLAUR Domain Containing 2 - Involved in cellular adhesion and signaling.
Chst2	2.383	0.026	Carbohydrate Sulfotransferase 2 - Regulates glycosylation and extracellular matrix remodeling.

Table 2. Top 20 downregulated genes in hamster lung following EV exposure

Gene	Log2 Fold Change	P-Value	Full Name and Function
Ube2d1	-1.626	0.00088	Ubiquitin Conjugating Enzyme E2 D1 - Involved in protein degradation and ubiquitin signaling.
C15orf48	-1.629	0.00225	Chromosome 15 Open Reading Frame 48 - Involved in immune response and inflammation.
Brms1l	-1.934	0.038	Breast Cancer Metastasis Suppressor 1-Like - Suppresses metastasis and regulates gene expression.
Nod2	-1.977	0.00088	Nucleotide-Binding Oligomerization Domain 2 - Pattern recognition receptor in immune response.
Rab5b	-2.02	0.0103	RAB5B, Member RAS Oncogene Family - Regulates endocytosis and intracellular trafficking.
Nrn1	-2.059	0.0195	Neuritin 1 - Promotes neuronal survival, plasticity, and repair.
Cd274	-2.087	0.00916	CD274 (PD-L1) - Immune checkpoint protein that inhibits T-cell activation.
Aoah	-2.132	0.0193	Acyloxyacyl Hydrolase - Detoxifies bacterial lipopolysaccharides to modulate inflammation.
Cxcr2	-2.397	0.0108	C-X-C Chemokine Receptor Type 2 - Receptor involved in neutrophil chemotaxis and inflammation.
Ms4a7	-2.633	0.0364	Membrane-Spanning 4-Domains A7 - Linked to immune cell function.
Tbx21	-2.827	4.64E-05	T-Box Transcription Factor 21 - Controls differentiation of T-helper cells.
Spp1	-2.861	0.0103	Secreted Phosphoprotein 1 - Osteopontin, regulates immune responses and tissue remodeling.
Dlx5	-3.163	0.0189	Distal-Less Homeobox 5 - Regulates bone and craniofacial development.
Mars2	-3.226	0.0177	Mitochondrial Methionyl-tRNA Synthetase 2 - Catalyzes aminoacylation of mitochondrial tRNA.
Lgals9	-3.459	0.0176	Galectin-9 - Modulates immune responses, apoptosis, and inflammation.
Prss35	-3.505	0.0305	Protease, Serine 35 - Involved in extracellular matrix remodeling and proteolytic activity.
Mrps10	-3.666	0.00181	Mitochondrial Ribosomal Protein S10 - Essential for mitochondrial protein synthesis.
Slc13a4	-6.006	0.0207	Solute Carrier Family 13 Member 4 - Sodium-dependent phosphate transporter.
Dmp1	-7.569	0.0152	Dentin Matrix Protein 1 - Involved in bone mineralization and phosphate regulation.
Ubl5	-9.245	4.51E-05	Ubiquitin-like Protein 5 - Regulates mitochondrial stress response and RNA splicing.

Table 3. Differentially expressed genes in EV exposed hamsters infected with SARS-COV-2.

Gene name	log2 Fold Change	p-value	p-adj	Full name and function
Nrn1	2.13	9.26E-05	0.033	Neuritin 1 | Promotes neuronal growth and survival, involved in nervous system development.
Pop7	2.10	0.0001536	0.045	Ribonuclease P Protein Subunit | Involved in tRNA processing.
Aqp3	1.97	3.36E-07	0.001	Aquaporin 3 | Water and glycerol channel important for cellular water homeostasis.
Mmp13	1.68	9.01E-07	0.001	Matrix Metalloproteinase 13 | Collagenase involved in extracellular matrix remodeling.
Mmp12	1.60	0.000104	0.036	Matrix Metalloproteinase 12 | Regulates elastin degradation in tissue repair and inflammation.
Dexi	1.52	6.98E-05	0.031	Dexamethasone-Induced Protein | Possibly involved in stress responses.
Pcbp1	1.48	8.90E-07	0.001	Poly(rC)-Binding Protein 1 | Regulates mRNA stability and translation.
Rps15a	1.45	7.32E-09	0.000	Ribosomal Protein S15a | Essential for ribosome assembly and protein synthesis.
Egln3	1.33	6.58E-05	0.031	Egl-9 Family Hypoxia-Inducible Factor 3 | Regulates cellular oxygen sensing and hypoxia response.
Irx5	1.29	0.0002307	0.052	Iroquois Homeobox 5 | Involved in developmental processes and cell differentiation.
Spp1	1.11	0.0002497	0.052	Secreted Phosphoprotein 1 | Key player in immune regulation and bone remodeling.
Egfl6	1.09	2.02E-05	0.015	EGF-Like Domain Multiple 6 | Involved in cell adhesion and angiogenesis.
Krcc1	1.07	3.28E-07	0.001	Kruppel-Related Zinc Finger Protein | Regulates transcription and chromatin remodeling.
Ndufb6	1.06	6.05E-06	0.005	NADH:Ubiquinone Oxidoreductase Subunit B6 | Component of mitochondrial complex I.
Golph3	0.97	4.12E-05	0.023	Golgi Phosphoprotein 3 | Regulates Golgi trafficking and cell growth.
Kctd5	0.85	7.86E-05	0.033	Potassium Channel Tetramerization Domain 5 | Involved in protein-protein interactions.
Zfp36l1	0.71	0.000181	0.048	Zinc Finger Protein 36 Like 1 | Regulates mRNA decay and inflammatory responses.
Smc4	0.66	0.0002219	0.052	Structural Maintenance of Chromosomes 4 | Involved in chromosome condensation and cohesion.
Pdap1	0.62	0.0001864	0.048	PDGFA-Associated Protein 1 | Regulates cell growth and proliferation.
Nsfl1c	-0.85	0.000126	0.041	NSFL1 Cofactor p47 | Involved in membrane trafficking and protein complex disassembly.
S1pr3	-0.89	0.0001868	0.048	Sphingosine-1-Phosphate Receptor 3 | Regulates vascular development, immunity, and inflammation.
Ndufaf3	-1.07	0.0001725	0.048	NADH:Ubiquinone Oxidoreductase Complex Assembly Factor 3 | Required for mitochondrial complex I assembly.
Fam20c	-1.31	2.45E-05	0.016	FAM20C Golgi Kinase | Regulates biomineralization and extracellular matrix homeostasis.
Serping1	-1.44	6.03E-05	0.030	Serpin Family G Member 1 | Regulates complement cascade and inflammation.
Slc31a1	-1.64	4.30E-14	0.000	Solute Carrier Family 31 Member 1 | Copper transporter important for cellular metabolism.
Gbp5	-1.77	9.22E-05	0.033	Guanylate Binding Protein 5 | Key player in innate immune response and inflammation.
Pex11g	-1.77	7.98E-07	0.001	Peroxisomal Biogenesis Factor 11 Gamma | Involved in peroxisome proliferation and metabolism.
Trnp1	-2.49	2.77E-10	0.000	TM1 Domain-Containing Protein 1 | Regulates neural stem cell proliferation and differentiation.

Table 4. Genes significantly regulated by EV in hamsters co-infected with IAV & SARS-COV-2.

Gene name	log2 Fold Change	p-value	Full name and function
Upregulated			
Crisp4	4.11	5.07E-03	Cysteine-Rich Secretory Protein 4 | Reproduction and immune response.
Map3k19	3.77	2.69E-03	Mitogen-Activated Protein Kinase Kinase Kinase 19 | Stress response regulator.
Myl3	3.62	4.97E-03	Myosin Light Chain 3 | Regulates cardiac muscle contraction.
Sco1	3.45	4.75E-03	Synthesis of Cytochrome C Oxidase 1 | Mitochondrial respiration assembly.
Cox8b	2.96	9.18E-03	Cytochrome C Oxidase Subunit 8B | Part of electron transport chain.
Hba-x	2.36	8.34E-03	Hemoglobin Subunit Alpha-X | Oxygen transport.
Cfap44	2.24	9.22E-04	Cilia and Flagella Associated Protein 44 | Function in ciliary movement.
Slc4a1	2.10	1.88E-03	Solute Carrier Family 4 Member 1 | Bicarbonate transport.
Marcks	2.00	1.37E-04	Myristoylated Alanine-Rich C-Kinase Substrate | Regulates actin cytoskeleton.
Neu2	1.98	8.88E-03	Neuraminidase 2 | Glycoprotein metabolism enzyme.
Mfap4	1.89	5.36E-04	Microfibril Associated Protein 4 | Connective tissue integrity.
Pop7	1.79	2.06E-03	POP7 Homolog | RNA and tRNA processing.
Tnni3	1.72	2.89E-03	Troponin I3 | Regulates cardiac muscle contraction.
Snca	1.65	1.13E-03	Synuclein Alpha | Implicated in neurodegenerative disease.
Pgls	1.59	2.90E-03	6-Phosphogluconolactonase | Involved in pentose phosphate pathway.
Polr3d	1.57	1.60E-03	RNA Polymerase III Subunit D | Transcribes small RNAs.
Pnpla2	1.53	3.18E-05	Patatin-Like Phospholipase Domain 2 | Lipid metabolism regulator.
Kif23	1.51	2.92E-03	Kinesin Family Member 23 | Essential for cytokinesis.
Klf9	1.49	6.71E-04	Kruppel-Like Factor 9 | Regulates cell differentiation.
Alpl	1.47	1.14E-03	Alkaline Phosphatase | Bone mineralization enzyme.
Washc1	1.29	6.10E-04	WASH Complex Subunit 1 | Actin cytoskeleton remodeling.
Arhgap35	1.21	1.50E-04	Rho GTPase Activating Protein 35 | Regulates cell migration.
Slc4a2	1.17	8.07E-03	Solute Carrier Family 4 Member 2 | Bicarbonate transporter.
Rps15a	1.16	3.31E-05	Ribosomal Protein S15A | Component of the ribosome.
Ube2g2	1.02	4.26E-03	Ubiquitin-Conjugating Enzyme E2 G2 | Mediates ubiquitination.
Tmem63b	1.00	5.89E-03	Transmembrane Protein 63B | Calcium ion transport.
c	0.91	6.45E-03	Ring Finger Protein 31 | Ubiquitin ligase activity.
Trim28	0.87	9.92E-03	Tripartite Motif Containing 28 | Chromatin remodeling and gene silencing.
Ackr1	0.81	9.26E-03	Atypical Chemokine Receptor 1 | Chemokine scavenger receptor.
Bcl2l13	0.77	5.66E-03	BCL2 Like 13 | Regulator of apoptosis.
Arl16	0.77	4.85E-03	ADP Ribosylation Factor-Like 16 | Intracellular trafficking regulator.
Tent5c	0.76	6.81E-03	Terminal Nucleotidyltransferase 5C | Adds nucleotides to RNA.
Eif3b	0.73	1.01E-03	Eukaryotic Translation Initiation Factor 3B | Translation initiation.
Ggh	0.72	1.96E-03	Gamma-Glutamyl Hydrolase | Folate metabolism.
Clba1	0.72	1.49E-03	Collagen Beta 1 | ECM structural protein.
Sptlc1	0.66	3.00E-03	Serine Palmitoyltransferase Long Chain Subunit 1 | Sphingolipid biosynthesis.

Downregulated			
Coa8	-0.57	6.21E-03	Cytochrome C Oxidase Assembly Factor 8 | Regulates mitochondrial respiratory function.
Taf10	-0.85	5.27E-03	TATA-Box Binding Protein Associated Factor 10 | Part of transcription initiation factor complex.
Sardh	-0.87	3.72E-03	Sarcosine Dehydrogenase | Catalyzes oxidative demethylation of sarcosine.
Pxmp2	-0.90	8.12E-03	Peroxisomal Membrane Protein 2 | Involved in peroxisomal transport.
Gabarapl1	-0.91	9.38E-04	GABA Type A Receptor-Associated Protein Like 1 | Autophagy-related protein.
Npr2	-0.97	7.43E-03	Natriuretic Peptide Receptor 2 | Regulates cGMP signaling and vascular tone.
Ranbp3	-1.07	3.30E-03	RAN Binding Protein 3 | Mediates nuclear export processes.
Ppp1r3c	-1.18	7.91E-03	Protein Phosphatase 1 Regulatory Subunit 3C | Regulates glycogen metabolism.
Hp	-1.32	3.70E-03	Haptoglobin | Binds free hemoglobin to prevent oxidative damage.
Pigq	-1.37	9.05E-03	Phosphatidylinositol Glycan Anchor Biosynthesis, Class Q | Essential for GPI-anchor synthesis.
Rrp15	-1.61	3.18E-03	Ribosomal RNA Processing 15 Homolog | Involved in rRNA maturation.
Gtf3a	-1.71	1.63E-03	General Transcription Factor IIIA | Zinc-finger protein involved in 5S rRNA transcription.
Fhod1	-1.71	4.17E-06	Formin Homology 1 Domain Containing 1 | Regulates actin cytoskeleton assembly.
Ctsa	-1.84	4.27E-03	Cathepsin A | Lysosomal enzyme involved in protein degradation.
Snrnp25	-1.94	1.62E-03	Small Nuclear Ribonucleoprotein 25 | Part of spliceosome for mRNA splicing.
Chrna1	-1.95	1.30E-03	Cholinergic Receptor Nicotinic Alpha 1 Subunit | Mediates synaptic transmission.
2610318N02Rik	-2.13	3.41E-03	Uncharacterized protein | Novel gene of unknown function.
Rpl3	-2.36	3.63E-03	Ribosomal Protein L3 | Component of the ribosome for protein synthesis.
Brf1	-2.43	2.45E-03	RNA Polymerase III Transcription Initiation Factor 1 | Regulates RNA polymerase III activity.
Zfp831	-4.16	8.63E-03	Zinc Finger Protein 831 | Putative transcriptional regulator.